9950-356

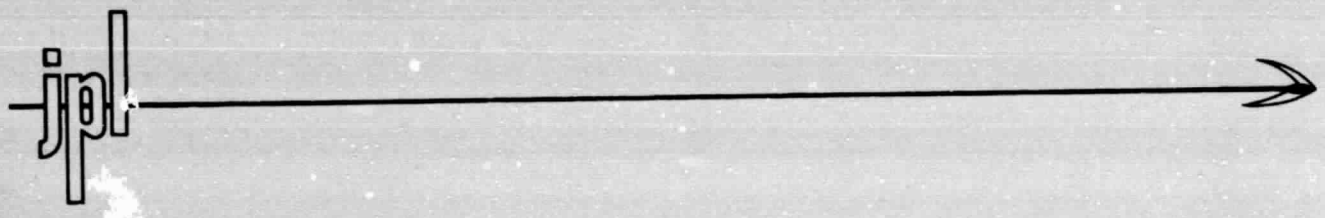

(NASA-CR-163040) FABRICATION AND SURFACE CHARACTERIZATION OF COMPOSITE REFRACTORY COMPOUNDS SUITABLE FOR THERMIONIC CONVERTERS Annual Report, 1 Aug. 1978 - 31 Jul. 1979 (Oregon Graduate Center for Study and) 81 p G3/24

N80-26399

Unclas 27868

JET PROPULSION LABORATORY

CALIFORNIA INSTITUTE OF TECHNOLOGY

PASADENA, CALIFORNIA

FABRICATION AND SURFACE CHARACTERIZATION OF COMPOSITE REFRACTORY COMPOUNDS SUITABLE FOR THERMIONIC CONVERTERS

Oregon Graduate Center
19600 N.W. Walker Road
Beaverton, Oregon 97005

FABRICATION AND SURFACE CHARACTERIZATION OF COMPOSITE REFRACTORY COMPOUNDS SUITABLE FOR THERMIONIC CONVERTERS

FABRICATION AND SURFACE CHARACTERIZATION OF COMPOSITE REFRACTORY COMPOUNDS SUITABLE FOR THERMIONIC CONVERTERS

ANNUAL REPORT

August 1, 1978 - July 31, 1979

December 1979

JET PROPULSION LABORATORY CONTRACT NO. 955156

Oregon Graduate Center
19600 N.W. Walker Road
Beaverton, Oregon 97006

P. R. Davis
L. W. Swanson

THIS WORK WAS PERFORMED FOR THE JET PROPULSION LABORATORY, CALIFORNIA INSTITUTE OF TECHNOLOGY SPONSORED BY THE NATIONAL AERONAUTICS AND SPACE ADMINISTRATION UNDER CONTRACT NAS7-100.

TABLE OF CONTENTS

		Page
I.	Introduction	1
II.	Characterization of properties of rare earth hexaboride surfaces--Task A	6
III.	Fabrication and characterization of Zr/W and Hf/W alloys--Task B	32
IV.	Characterization of cesiated surfaces of promising electrode materials--Task C	50
V.	Summary	72
	References	75

I. Introduction

The objective of the JPL thermionics program is to establish the feasibility of an advanced lightweight, long-life, direct energy conversion system compatible with a nuclear reactor or solar heat source. The principal application foreseen at this time is the use of nuclear power for electric propulsion. Other applications of direct energy conversion that will benefit from this program include nuclear and solar thermionic/thermoelectric power for Earth orbital and lunar applications, as well as terrestrial topping cycle applications.

The objective of the OGC program in thermonics is to fabricate, characterize and evaluate new electrode materials that have the potential of significantly improving converter performance. The underlying philosophy of this work can be summarized in the following assumptions:

(1) an emitter material for advanced mode TEC operation should exhibit both a low clean work function (2.1 to 3.0 eV) and low volatility;

(2) the collector electrode work function should be as low as can be tolerated by back emission considerations; and

(3) it would be desirable to have an emitter and collector of the same material.

Historically the emitter electrode has possessed a high clean surface work function. The advantage of a low clean surface emitter work function is its ability to exhibit high emitter current density levels at relatively low temperature (e.g. 10 A/cm^2 at 1626 K for LaB_6) without any Cs pressure. This important advantage allows one

to reduce the converter cesium pressure and hopefully eliminate or greatly reduce the vacuum arc drop, yielding much greater flexibility in converter design. In addition, it has been suggested that low work function electrode materials such as LaB_6 may greatly increase TEC efficiencies and result in higher power outputs at ~ 1700 K.[1]

For these reasons, the OGC program has paid particular attention to the techniques of fabricating and characterizing the surface properties of promising new electrode materials. Our objective has been to gain a clearer understanding of the basic surface properties of these materials in relation to their utilization as thermionic energy converter electrodes. We will continue to emphasize the study of those factors (e.g., cesium desorption kinetics and mechanisms of low work function production) which are of primary concern to successful thermionic converter performance.

During the past year we have assessed the relevant surface properties of some promising rare earth hexaboride (RB_6) electrode materials and investigated zirconium/tungsten and hafnium/tungsten alloys. At present our surface analysis techniques include Auger electron spectroscopy, mass spectroscopy of surface desorption products, field emission retarding potential (FERP)[2] technique of measuring work function and electron reflection, field electron and ion microscopy and low energy electron diffraction (LEED).

Two important considerations in the selection of an appropriate emitter electrode material are its work function and volatility.

In the case of the cesium thermionic diode it is important to know the variation of emitter work function ϕ_e with temperature T_e and cesium pressure P_{cs}. Then the emitted current density J_e may be determined as a function of these operational parameters. It is entirely equivalent to determine the functional dependence of the cesium coverage $\sigma = \sigma(T_e, P_{cs})$ and the dependence $\phi_e = \phi_e(\sigma)$, which may be done using thermal desorption mass spectrometry and FERP.

Volatility of the emitter electrode at the operating temperature should be as low as possible in order to minimize contamination of the collector electrode. In the case of identical emitter and collector materials this may not be a significant problem. For binary electrode materials such as LaB_6 or CeB_6 it is now known that, within certain stoichiometric limits, the volatility is minimized and the evaporation occurs congruently so that emitter material condensing on the collector should not alter its composition.[3]

During the past year we have begun studies of a new class of promising refractory materials which consist of dilute alloys of zirconium or hafnium in tungsten or molybdenum. Certain crystal faces of these alloys are known to produce low (~ 2.6 eV) work function surfaces which are unusually stable at elevated temperature (~ 2000 K).[4,5] Work in this laboratory during the past four years has shown that as a thermal field electron source the Zr/W alloy emitter can operate in excess of 5000 hours at 1800 K. Little is yet known regarding the mechanism by which these bulk alloy materials produce low work function surfaces or the optimum alloy

compositions, although we have demonstrated that polycrystalline W - 5% Hf and W - .5% Hf alloys, when annealed in vacuum, show surface enrichment of hafnium and significant average work function decrease. Further work on this class of bulk alloys should concentrate on thermal treatment to develop the lowest work function surface planes (100), and optimization of bulk hafnium or zirconium concentration.

An unusual property of these systems is their strong affinity toward oxygen. On pure tungsten, tungsten oxide surface layers are removed at 1800 K. With small amounts of zirconium present, however, temperatures in excess of 2200 K are required to remove oxygen from the surface. It is now clear that oxygen promotes the bulk diffusion of zirconium in tungsten in the form of a Zr-O complex.

One of our major accomplishments during the past year has been a detailed study of zirconium and oxygen coadsorption on the (100) plane of tungsten. This model alloy system provides an ordered surface which lends itself to characterization by surface-sensitive techniques. These studies have yielded insight into the nature of the low work function surface and methods of routinely achieving the low work function on this plane have been developed.[5]

In order to evaluate the prospects of the above mentioned electrode materials for advanced mode converter operation a diode TEC consisting of a pressed and sintered LaB_6 emitter and collector has been recently evaluated at the NASA Lewis Research Center.[6] The results thus far are very encouraging even though the performance has not been optimized with respect to Cs reservoir pressure

and diode spacing. Although the Cs pressure could not be established, the results summarized in Table I give a remarkably low barrier index of 1.9 eV. This enhanced performance could not be duplicated in subsequent tests at Thermo Electron Corporation under JPL contract.

TABLE I

Cs Diode Performance Using LaB_6 Electrodes

Efficiency	16%
Emitter Temperature	1696 K
Collector Temperature	853 K
Power Density	3.8 W/Cm
Output Voltage	0.7 V

These preliminary TEC results using a refractory, low work function material such as LaB_6, even though unoptimized with respect to operating parameters and electrode fabrication techniques, provide evidence that considerable improvement in converter performance can be expected. Further converter studies using the appropriate single crystal electrodes of LaB_6 and CeB_6, which have been characterized in our present program, should yield additional improvement in converter performance. Practical problems associated with fabrication of these electrode materials have been, for the most part, solved for small scale R & D evaluation of converter performance, although there are still difficulties in bonding RB_6 materials and maintaining physical stability. With additional effort methods of fabrication and mounting these electrode materials (taking advantage of the crystallographic anisotropies) for practical scale TEC manufacture should be feasible. For example, CVD and plasma

spraying on suitable substrates are possible electrode fabrication approaches to be considered.

The research program we have pursued during the past year can be conveniently separated into three major tasks:

Task A: Characterization of electronic, compositional and structural properties of rare earth hexaboride surfaces

Task B: Fabrication and characterization of Zr/W and Hf/W alloys

Task C: Characterization of cesiated surfaces of promising electrode materials

We shall discuss the results obtained under each task individually.

II. Characterization of properties of rare earth hexaboride surfaces - Task A

Work on rare earth hexaboride characterization during the past year has concentrated on detailed study of a few samples. In order to eliminate nonuniformity of surface properties, we have used single crystal samples of precisely known stoichiometry and surface orientation. These samples, supplied by Dr. John Verhoeven of Iowa State University, were cut from triple zone refined material of $LaB_{5.74 \pm .03}$ bulk stoichiometry with less than 70 ppm bulk impurities.[7] The specimens were oriented in (100), (110) and (321) directions, respectively, and the surfaces to be studied were mechanically polished with 600 grit SiC powder. The $LaB_{5.74}$ composition allowed comparison with previous results on samples less rich in La.[8]

The study of single crystal specimens of La-rich composition promised to be particularly fruitful. To begin with, examination of surfaces of different orientation can help to identify those orientations which have the most desirable properties for converter applications, i.e., low volatility and low electronic work function. Previous studies[8] have shown that, among the low index planes of LaB_6, the (100) plane exhibits the lowest thermionic work function, while the (111) has the highest work function. High index planes, such as (321) and (346) may have surface properties that vary with heat treatment, and may even rearrange during heating in vacuum to form facets of higher symmetry. The low index planes appear to be thermally stable in vacuum. The (346) plane has been shown to exhibit a (hot) thermionic work function less than that of the (100) but a (cold) retarding potential work function comparable to that of the (111). A recent study showed that, during heating in O_2 the stable plane of LaB_6 is the (100) with the (110), for example, forming facets of (100) orientation.[9]

The variation of work function among different crystal faces is a phenomenon observed for all types of materials, including metal single crystals. One might expect, however, that the situation is less complicated for single component systems than it is for systems such as LaB_6, where the surface composition as well as the surface structure may affect the work function. Table II is a summary, compiled by Swanson, et al.,[8] of the Richardson work function values, measured by various investigators, of several different crystal planes

of LaB_6. Note that there is a broad variation among values for a given crystal plane. Some of the variation may be attributed to differences in sample stoichiometry, and there may also be an effect caused by adsorption of background gases during the measurements. Both these possibilities will be discussed later.

Table II

Summary of Richardson Work Function Values of Various Crystal Planes of LaB_6*

Plane	ϕ(eV)	P (torr)**	Ref.
001	2.52 ± .05	5×10^{-10}	8
001	2.47 ± .06	5×10^{-10}	10
001	2.4 ± .2	$< 2 \times 10^{-7}$	11
001	2.8	2 to 7 $\times 10^{-8}$	12
001	$\geq$ 3	5×10^{-7}	13
011	2.60 ± .05	9×10^{-10}	8
011	2.5	5×10^{-7}	13
011	2.6	2 to 7 $\times 10^{-8}$	12
011	2.74	$< 1 \times 10^{-9}$	14
111	2.90 ± .05	5×10^{-10}	8
111	3.4	2 to 7 $\times 10^{-8}$	12
123	2.3 ± .2	2×10^{-7}	11
346	2.41 ± .05	5×10^{-10}	8

*Nominal sample composition. The samples studied in Ref. 8 had precisely known bulk stoichiometry of $LaB_{5.85}$.

**Base pressure during measurement.

Work function data for the $LaB_{5.74}$ single crystal surfaces studied in this work are presented in Table III. Both FERP and "effective" thermionic work functions are given. The "effective" work function is determined by solving the Richardson equation

$$J_o = 120\ T^2 \exp(-\phi_{eff}/kT) \qquad (1)$$

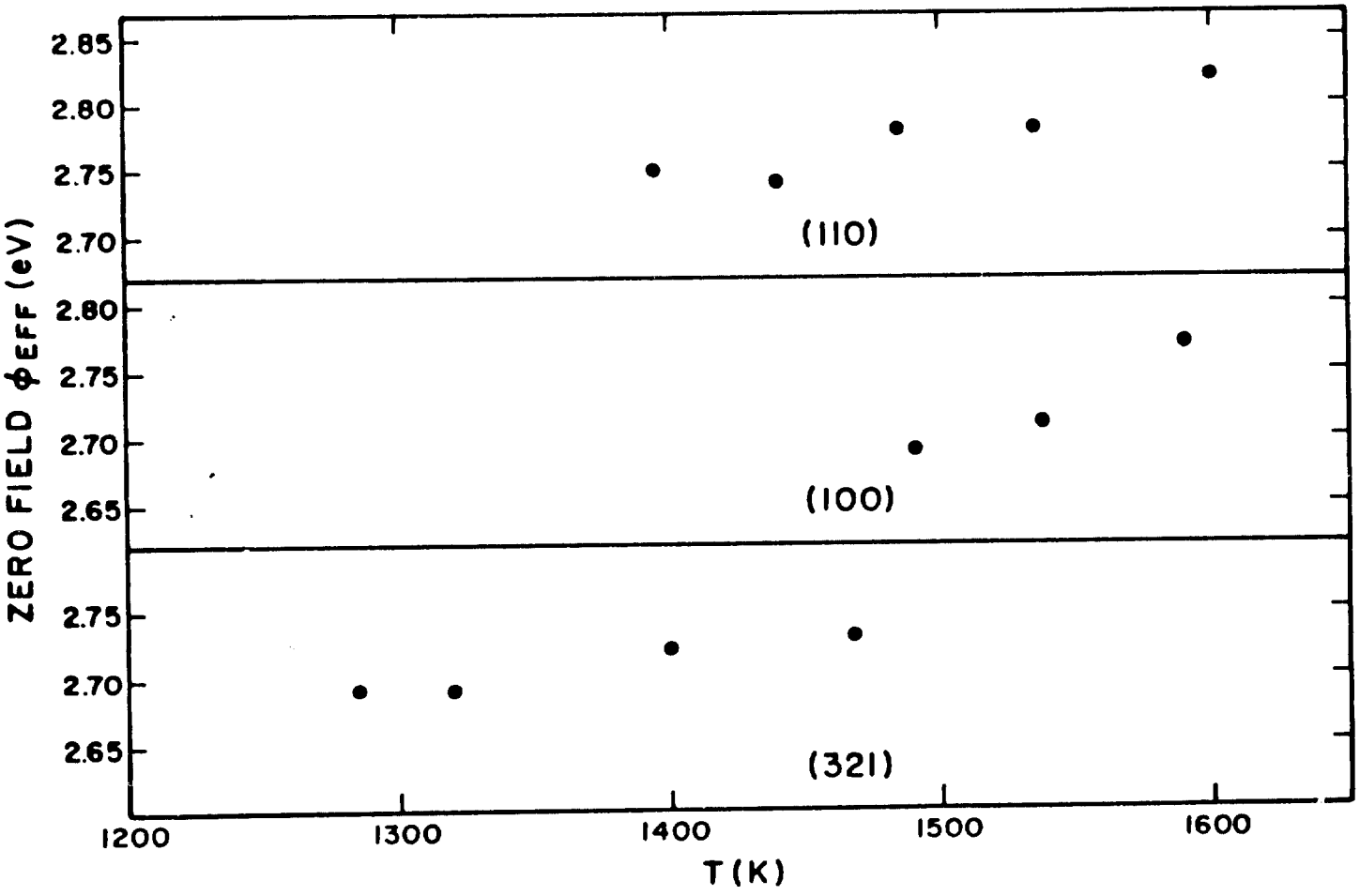

Figure 1. Temperature variation of thermionic work functions of various crystallographic planes of $LaB_{5.74}$.

for ϕ_{eff}, given a measured zero-field current density J_o and corresponding temperature T. This procedure eliminates ambiguities caused by variation in slope of a $\ell n(J_o/T^2)$ vs $1/T$ plot. The temperature variation of ϕ_{eff} for these three planes is shown in Fig. 1. It can be seen that ϕ_{eff} tends to increase with temperature ($1300 \leq T \leq 1600$ K)

Table III

Measured zero field effective thermionic work functions (ϕ_{eff}) and FERP work functions (ϕ_{FERP}) of $LaB_{5.74}$ single crystal surfaces.*

Surface	ϕ_{eff} (eV)** at T(K)		ϕ_{FERP} (eV)***
(100)	2.74 ± .05	1600	2.70 ± .05
(110)	2.82 ± .05	1600	2.80 ± .05
(321)	2.76 ± .05	1600	2.95 ± .05

*Measured after heating only enough to clean the surface of contamination.

**Calculated from pulsed mode current density measurements (6×10^{-4} duty factor) assuming pre-exponential constant of 120 A - cm^{-2} - K^{-2}.

***Corrected peak position in derivative plot of collected current.

for all three surface planes. Similar behavior was observed previously[15] for (110), (346), (111) and (100) surfaces of samples with bulk stoichiometry of $LaB_{5.85}$. In that same study, however, the (100) surface showed essentially no temperature variation of ϕ_{eff} after extended heating in the range $T \lesssim 1800$ K, suggesting a strong effect from changing surface stoichiometry.

In Table III, there are striking differences between ϕ_{eff} and ϕ_{FERP} for the (110) and especially for the (321) surface. This effect may be due to two possible mechanisms. The FERP measurement yields a value for ϕ which is geometrically averaged over the surface, whereas ϕ_{eff} is strongly weighted toward the lowest work function of the surface. This difference is of little consequence if the surface is uniform, but may yield significantly different values if facetting of the surface occurs. Thus, for example, if the (321) surface facets to regions of low work function and high work function then one would expect ϕ_{eff} to be lower than ϕ_{FERP} for this plane.

A second mechanism is change of surface composition with temperature. The trend indicated in Fig. 1, i.e., higher ϕ_{eff} at higher temperature for $T \gtrsim 1300$ K, clearly cannot be extrapolated to room temperature where ϕ_{FERP} measurements are made. Another technique must be employed. We have studied the effect of temperature upon the ratio of boron to lanthanum in the surface region by means of Auger electron spectroscopy (AES). This method gives only a qualitative idea of the surface stoichiometry at different temperatures, because AES samples the first three or four atomic layers of the surface region, whereas the work function itself is strongly dependent upon the composition of the outermost atomic layer. A dramatic change in AES B/La ratio, however, can be interpreted as a change in surface stoichiometry which could be reflected in a work function change.

In Table IV we present data obtained in this study and in previous work showing the effect of heating on the B/La ratio for various

Table IV

Temperature dependence of Auger peak ratios

Surface	T = 300 K		1000 ≤ T ≤ 1700 K		Change During Heating (%)	
	B(179)*/La(78)	B(179)/La(625)	B(179)/La(78)	B(179)/La(625)	B(179)/La(78)	B(179)/La(625)
(100)**	1.7	4.2	1.5	4.7	-11	+12
(110)**	2.0	3.3	1.3	5.5	-35	+67
(321)**	2.0	6.0	1.8	5.2	-10	-13
(100)a***	9.3 ± .3	2.0 ± .5	2.3 ± .3	4.0 ± .1	-75	+100
(100)b***	.95 ± .05	4.6 ± .1	1.0 ± .1	4.0 ± .1	~ 0	-13
(111)***	1.3 ± .1	6.1 ± .1	1.3 ± .2	5.9 ± .1	~ 0	-3
(110)***	1.3 ± .1	4.1 ± .1	1.4 ± .1	4.0 ± .1	~ 0	~ 0
(346)***	1.2 ± .1	5.0 ± .1	1.25 ± .05	4.8 ± .1	~ 0	-4

*Numbers in parentheses indicate energies of Auger transitions monitored.
**This study. Bulk stoichiometry $LaB_{5.74}$. AES measurements made using 3 keV, 10 μA beam, 2V p-p modulation. Samples heated only enough to clean surfaces.
***Ref. 15. Primary beam energy 5 keV. Bulk stoichiometry $LaB_{5.85}$.
a - After initial thermal cleaning.
b - After prolonged heating at 1800 K.

crystal planes of zone refined LaB_6 samples. Large changes in B/La surface ratio during heating are observed only for the (110) crystal used in the present study and for a (100) specimen examined previously[15] which had been heated for only a short time.

The results of Storms and Mueller[3,16] and Kudintseva, et al.,[17] indicate that the work function of polycrystalline LaB_x is highly sensitive to surface composition. The surface composition, in turn, is a complicated function of the bulk stoichiometry and the temperature, and is determined in the non-equilibrium case of free vaporization by competition between bulk diffusion and desorption rates

of vaporizing species. The effect of crystallographic orientation on these rates has not been studied, nor has the effect of surface composition on the work functions of single crystal surfaces. We might expect that single crystal surface work functions should be sensitive to surface composition in much the same way as for polycrystalline surfaces. A comparison of Tables III and IV suggests, however, that no direct correlation exists between B/La ratio and work function, even for the same sample at different temperatures.

Recent results have indicated that very low levels of carbon contamination (a few percent) may affect the work functions of LaB_6 surfaces to a greater extent than would be expected on the basis of past experience with metal surfaces. Future studies of the effect of carbon may help explain change of LaB_6 work functions with extended heating.

A second important parameter, besides work function, which must be determined for materials to be used in converter cathode applications is volatility at operating temperature. Previous studies have shown that, for polycrystalline LaB_x, the lowest volatility occurs at the congruently vaporizing composition (CVC), $6.04 \lesssim x \lesssim 6.07$, corresponding to La and B desorption activation energies of about 6.3 eV for Langmuir (free) vaporization.[3] It is also known that the overall sample volatility can be strongly increased by the presence of background gases (such as O_2) in the vacuum or impurities in the sample.[3] We have therefore made measurements of the activation energies of free

vaporization and the effects of oxygen partial pressure on overall sample volatility for the $LaB_{5.74}$ samples.

The free vaporization measurements were made on $LaB_{5.74}$(100), $LaB_{5.74}$(110) and $LaB_{5.86}$(110). The results of these measurements are given in Table V, along with those from a previous study of a $LaB_{5.86}$ (346) crystal.[18] Thus, the effects on vaporization of stoichiometry and crystal orientation can be separated. Comparison of the results in Table V suggests that, at least for La-rich material, the activation energy of free vaporization of La is unaffected by crystal orientation while the corresponding energy for B is strongly dependent upon surface structure. The $LaB_{5.86}$(110) and (346) crystals showed much higher La vaporization energies than either of the $LaB_{5.74}$ samples. This behavior is in excellent agreement with the polycrystalline data of Storms and Mueller[3] if $LaB_{5.74}$ and $LaB_{5.86}$ exist in a single phase region as has been concluded by Noack[7] from density measurements on these materials. The $LaB_{5.74}$(110), $LaB_{5.86}$(110) and $LaB_{5.86}$(346) B vaporization energies also agree well with the polycrystalline data of these authors, but the $LaB_{5.74}$(100) value differs significantly, suggesting that the B vaporization energy has a strong crystallographic dependence.

The conclusion that may be drawn from these free vaporization measurements on La-rich single crystal samples is that, while La evaporation may be fixed by sample stoichiometry and operating temperature, total evaporation (La + B) may be adjusted by choosing crystalline geometry such that low B-evaporating faces are exposed. It is indeed fortunate that the (100) face apparently has both properties

Table V

Activation energies for free vaporization of B and La from clean, La-rich LaB_6 single crystal samples

Sample*	Activation Energy of free vaporization B	La
$LaB_{5.74}(100)$**	7.2 ± .2	4.3 ± .1
$LaB_{5.74}(110)$**	6.2 ± .1	4.3 ± .1
$LaB_{5.86}(346)$***	6.4 ± .1	5.4 ± .1
$LaB_{5.86}(110)$**	5.7 ± .2	5.1 ± .1

*Preparation and analysis of all three samples discussed in Ref. 7.
**This work
***Ref. 18

desirable for converter applications, i.e., low work function and low B (and consequently low total) evaporation.

Total mass loss of a LaB_x crystal may be affected strongly by the presence of active gases at the hot surface. We have therefore investigated, in detail, the interaction of oxygen with a $LaB_{5.74}(100)$ surface. This study was performed in two parts: first, thermal desorption studies yielded information on the nature of surface oxide species and their thermal removal characteristics under negligible oxygen partial pressure ($P_{O_2} < 1 \times 10^{-10}$ torr) conditions. These non-equilibrium experiments allowed high-sensitivity mass spectrometric measurements to be made on desorbing species. Second, steady-state measurements in various fixed pressures of oxygen provided more detailed information on the

kinetics of formation and removal of the various oxide species under conditions similar to those of actual converter operation.

The thermal desorption measurements were performed after the sample was dosed and cooled to 300 K and the total chamber pressure had returned to below 1×10^{-9} torr. The EAI 250 mass spectrometer used in these studies had a resolution of 0.5 amu over the mass range 2-150, and 1 amu up to mass 500. Temperatures were measured using a W-5%/W-26% Re thermocouple spotwelded to the sample support. The thermocouple was calibrated against optical pyrometer measurements in the range 1000-2000 K, and desorption spectra were made using a linear heating current increase with time, yielding a nonlinear temperature-time curve.

A summary of the species monitored and those observed is given in Table VI. Figure 2 shows desorption spectra obtained after O_2 adsorption of 4×10^{-5} torr-sec at 1000 K. While LaO^+, BO^+ and $B_2O_2^+$ were observed after 2×10^{-6} torr-sec O_2 exposure, $B_2O_3^+$ desorption did not occur for exposures less than 1×10^{-5} torr-sec. Only the high energy peak in the BO^+ spectrum was observed after exposures up to 1×10^{-5} torr-sec, while the lower energy peak appeared for larger doses. Adsorption to saturation at room temperature yielded spectra identical to those observed for 1×10^{-5} torr-sec exposure at 1000 K. Exposure to doses greater than 1×10^{-5} torr-sec at 1000 K caused additional BO and B_2O_2 binding states to form, and small quantities of B_2O_3 were then observed by thermal desorption spectroscopy.

TABLE VI

Thermal Desorption of Oxides from $LaB_{5.74}(100)$: Species Monitored

Mass (species)	Conditions of Detection	Comments
139 (La^+)	$T \gtrsim 1470$ K, clean or oxygenated sample	Shows fragmentation peak from LaO when surface is oxygenated
69.5 (La^{++})	Same as La^+	
326 ($La_2O_3^+$)	Not observed	
294 (La_2O^+)	Not observed	
171 (LaO_2^+)	Not observed	
155 (LaO^+)	Observed whenever the LaB_6 surface has any oxygen present, regardless of adsorption temperature	
77.5 (LaO^{++})	Same as LaO^+	
70 ($B_2O_3^+$)	Observed after adsorption at $T \gtrsim 1000$ K only with exposure $\gtrsim 10$ L. Not observed after room temperature oxygen adsorption.	Broad peak, may be second order, but coverage dependence has not been studied in detail.
54 ($B_2O_2^+$)	Observed after adsorption at 300 K or 1000 K at any oxygen exposure	Appears to be the dominant B oxide species desorbed.
43 (BO_2^+)	Not observed above background	
27 (BO^+)	Observed after any oxygen exposure at 300 K or 1000 K	Single peak observed after 2L O_2 adsorption, multiple peaks after $>$ 10L O_2 dose at 1000 K.
11 (B^+)	$T \gtrsim 1630$ K, clean or oxygenated sample	When oxygen is present on the surface, lower temperature peaks from fragmentation of boron oxides are observed
32 (O_2^+)	Not observed above system background	
16 (O^+)	Not observed above system background	

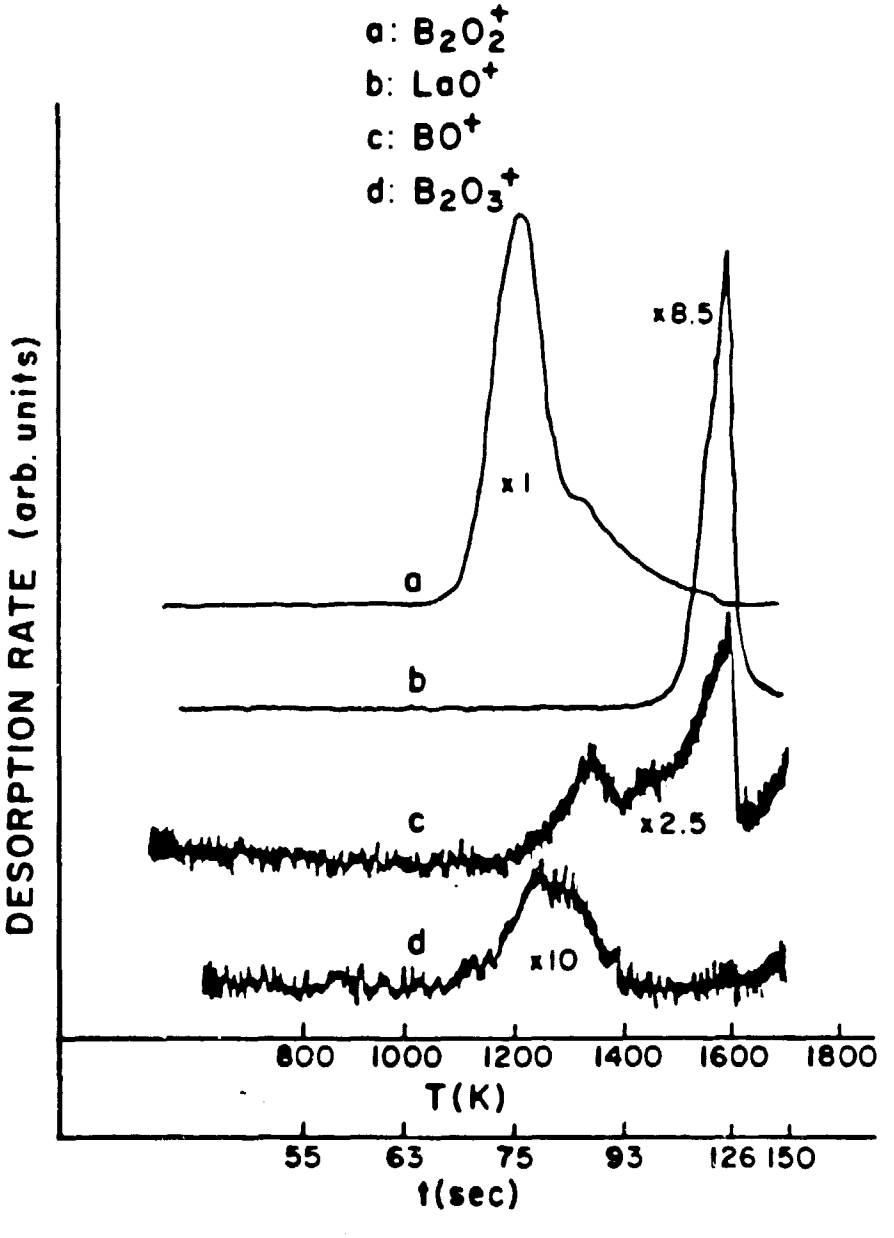

Figure 2. Desorption spectra of various oxide species from $LaB_{5.74}$(100) after 4×10^{-5} torr-sec oxygen exposure at 1000 K.

These results are in disagreement with the work of Swanson and Dickinson[10] and Goldstein and Szostak,[19] who observed only $B_2O_3^+$ and LaO^+, respectively. On the other hand, our results are similar to the observations of Bas, et al.,[9] for O_2 on $LaB_6(110)$, although the latter authors did not observe $B_2O_3^+$ nor $B_2O_2^+$ desorption.

The desorption energies of the observed oxide species were determined by the Redhead technique[20] with the assumption of first-order desorption in all cases. Over a given small range, the heating rate was approximately linear, so that this technique could be applied. The results of these desorption energy calculations are shown in Table VII. Note that the LaO and BO binding energies determined in this study are very close to those measured by Bas, et al.,[9] even though the samples have different surface geometry and presumably different bulk stoichiometry.

From Figure 2, one can clearly see an important result: significant desorption of boron oxides occurs at temperatures well below the onset of LaO desorption. The onset of B_2O_2 desorption is $T \lesssim 1100$ K. In turn, elemental La evaporation occurs for $T \gtrsim 1470$ K, while elemental B evaporation begins at $T \approx 1630$ K. Thus, for $1100 \lesssim T \lesssim 1500$ K one would expect an oxidized layer on the $LaB_{5.74}(100)$ surface to become B depleted. Since a nominal $LaB_6(110)$ crystal[9] exhibits BO and LaO desorption behavior similar to what we have observed for $LaB_{5.74}(100)$ one might guess that, in general, boron oxides tend to be less strongly bound to LaB_6 surfaces than are lanthanum oxides. We therefore performed

TABLE VII

Thermal Desorption of Oxides from LaB_6: Binding Energies

Species	Binding Energy (eV)[1] This Work $LaB_{5.74}(100)$[2]	(a) $LaB_6(100)$[3,4]	(b) $LaB_6(110)$[3,5]
LaO	4.3 ± .2[6]	5.5	4.2
BO	3.6 ± .1[7]	---	3.4 3.9
	4.3 ± .1		4.1
B_2O_2	3.3 ± .1[8] 3.5 ± .1	---	---
B_2O_3	3.4 ± .1	---	---

(a) Ref. 19
(b) Ref. 9

1. Binding energies of oxide species determined by Redhead method.
2. After O_2 adsorption at 1000 K.
3. Nominal composition.
4. Apparently measured in continuous O_2 background pressure - clean sample claimed. LaO binding energy determined from Arrhenius plot.
5. After O_2 adsorption at 300 K.
6. Peak broadens toward low temperature at highest O_2 doses.
7. Low energy peak not present for O_2 dose < 1×10^{-5} torr-sec.
8. Exposures > 20L cause a lower energy state to form. After 200L at 1000 K, for example, desorption from this third state is observed for T > 1000 K.

preliminary steady-state oxide evaporation measurements on the $LaB_{5.74}(100)$ surface in oxygen pressures up to 5×10^{-6} torr, in order to study this boron depletion phenomenon in more detail.

The oxide evaporation studies in O_2 pressures utilized both mass spectrometric analysis and Auger electron spectroscopy. Thus, it was possible to characterize desorbing species and to study the nature of the sample surface itself. The combination of these two techniques

yielded more complete information on the oxidation process than either technique alone could provide.

Some limitations on the mass spectrometric measurements were imposed by the presence of a high O_2 pressure. Several possible evaporating species could not be monitored because of overlap in the mass spectra from identical or nearby species present in the gas. For example, O^+ (mass 16) and O_2^+ (mass 32) could not be detected as desorbing from the sample, because the background yield of these ions was orders of magnitude larger than the expected desorbing yield. Similarly, overlap of CO^+ (mass 28) with BO^+ (mass 27) made detection of the latter virtually impossible. On the other hand, steady-state yields of desorbing species with no background interference were high enough to allow techniques such as isotopic fingerprinting to be applied. For example, it was possible to identify $B_2O_2^+$ unequivocally by use of the known boron isotopic distribution (~ 80% B^{11}, ~ 20% B^{10}) to compare the calculated and measured ratios of $B_2^{10}O_2$ (mass 52), $B_2^{10}B^{11}O_2$ (mass 53) and $B_2^{11}O_2$ (mass 54). Agreement within 3% was obtained in this experiment.

Figures 3-5 show typical results of measurement of the yield of a given species, at a given temperature (1600 K) as a function of oxygen pressure in torr. Note that the data for elemental boron (Figure 3) are best fit by a straight line of slope 1.21 on a dual logarithmic plot, whereas the B_2O_2 data (Figure 4) are fit well by a straight line on a linear plot. The B_2O_2 vaporization data fall on a straight line in a semilog plot (Figure 5). It is known[21] that one of the stable bulk boron oxides, $(BO)_x$, decomposes to form B_2O_2 on heating. The other stable boron oxide is B_2O_3.

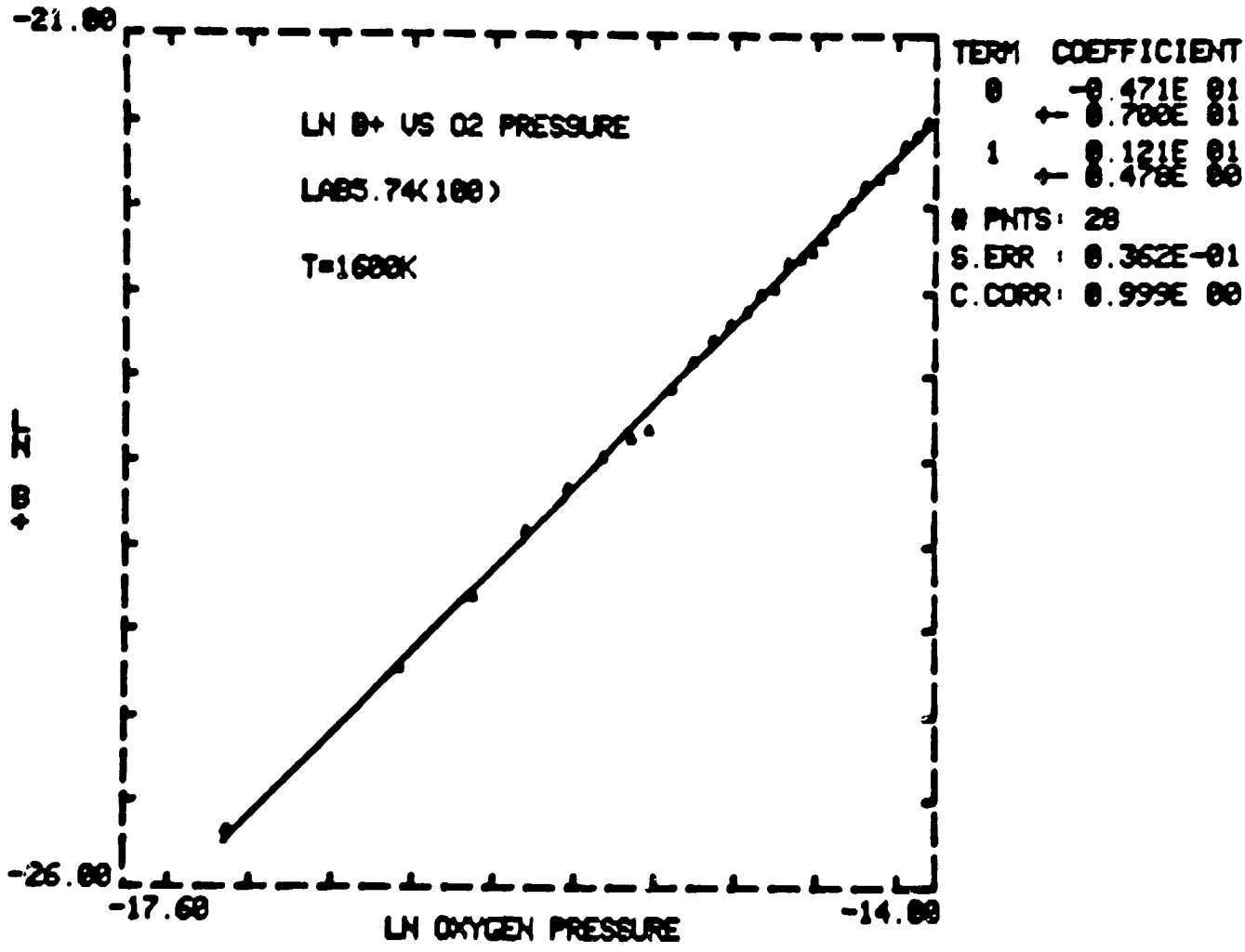

Figure 3. Natural logarithm of B^+ signal from $LaB_{5.74}(100)$ vs natural logarithm of oxygen pressure at 1600 K. The B^+ signal arises from fragmentation of B oxide species.

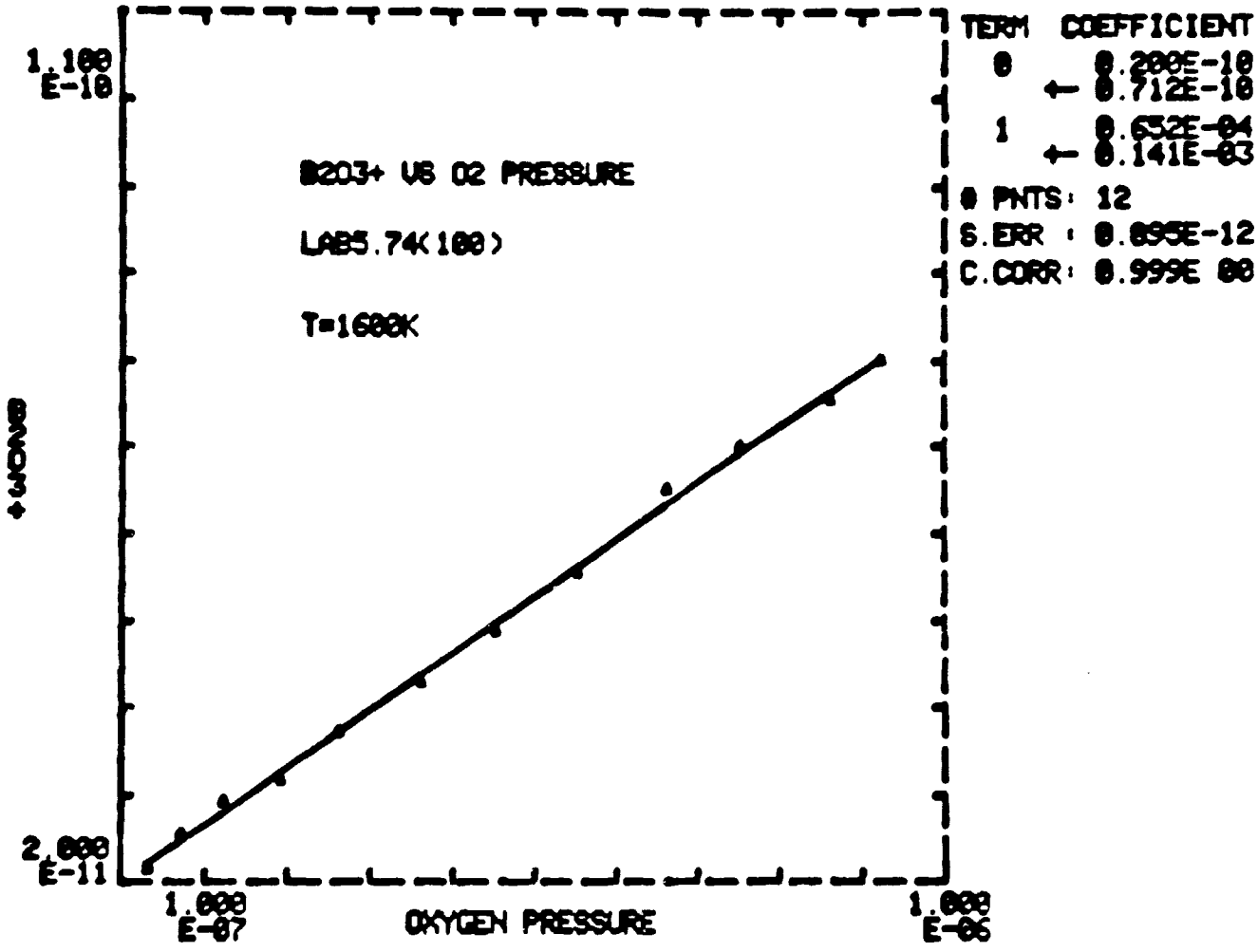

Figure 4. $B_2O_3^+$ signal from $LaB_{5.74}(100)$ as a function of oxygen pressure at 1600 K.

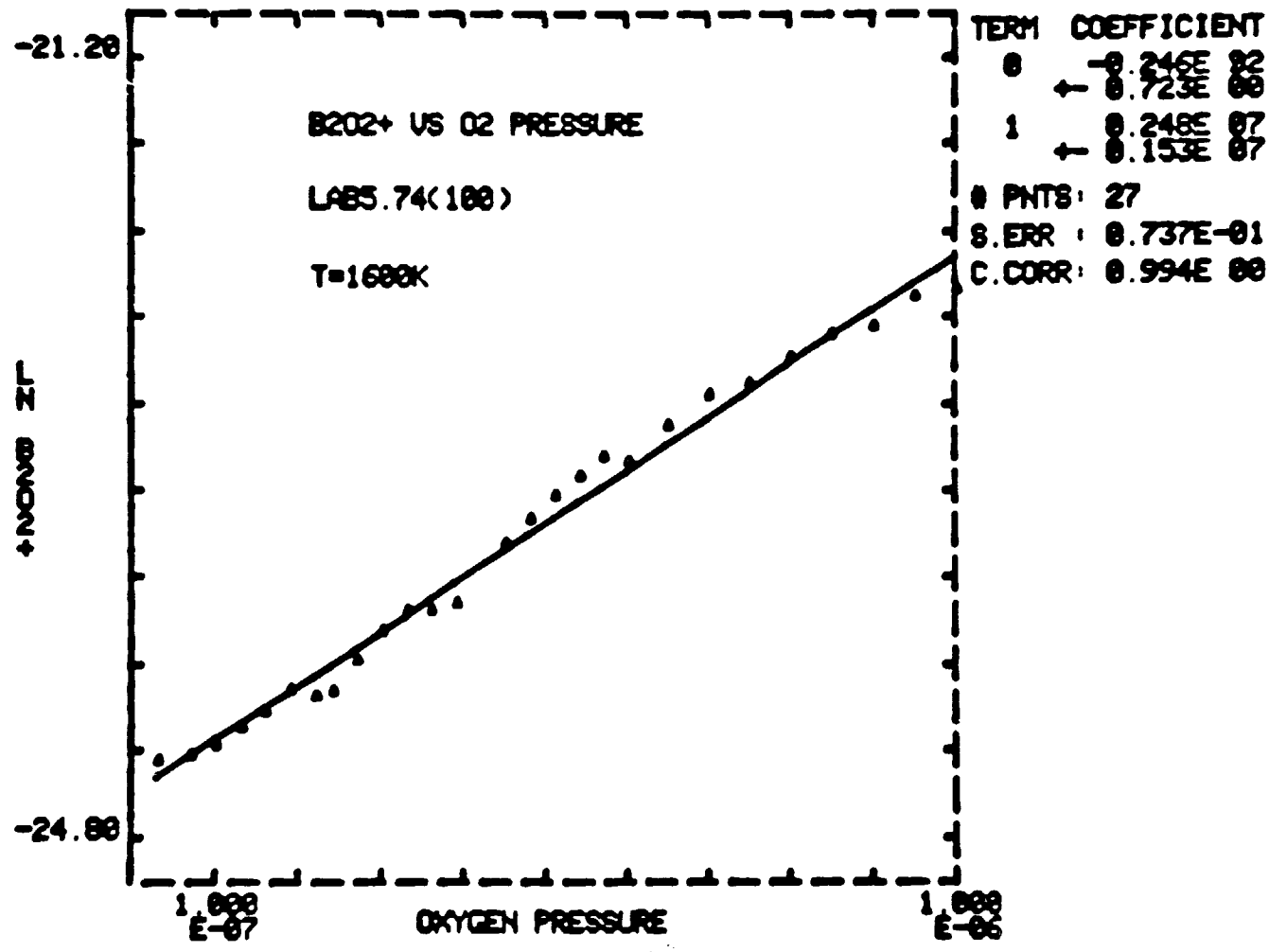

Figure 5. Natural logarithm of $B_2O_3^+$ signal from $LaB_{5.74}(100)$ as a function of oxygen pressure at 1600 K.

Because of the apparent complex nature of the reactions producing B_2O_2 and B_2O_3, it seems unlikely that the kinetics can be described in detail. Most probably, the rate of B_2O_2 production depends on the concentration of BO at the surface, since B_2O_2 might be formed by the reaction

$$2\ BO \rightleftarrows B_2O_2$$

The concentrations of the various species on the surface cannot, at present, be measured, nor can the formation rate of BO from elemental B and O be determined. In fact, even the reaction producing BO must involve several steps, i.e., adsorption of O_2, dissociation of O_2, dissociation of LaB_6 and final reaction of B and O. Formation of detected B_2O_2 and B_2O_3 are even more complicated, involving additional reaction steps and finally desorption. At each step there are likely to be several possible reaction paths. It is therefore intriguing that the measured desorption rates of the various boron species depend on the O_2 pressure in apparently simple ways.

The relative overall boron removal rate can be determined by correcting for the mass sensitivity of the quadrupole spectrometer, and assuming that ionization probabilities of all the boron species are the same and that the elemental B peak is due exclusively to cracking in the 70 eV ionizer beam. In addition, an assumption has to be made about the relative amount of BO desorbing, since this species cannot be measured in an O_2 pressure. If negligible BO is desorbed, and most of the BO goes to the formation of B_2O_2 and B_2O_3,

we obtain the curve shown in Figure 6, where the data for the individual species are replotted along with the total boron. The total boron removal rate depends strongly upon the oxygen pressure, in the range $5 \times 10^{-8} \lesssim T \lesssim 1 \times 10^{-6}$ torr for a sample at T = 1600 K.

The rates of removal of the oxides B_2O_2, B_2O_3 and LaO have also been measured as functions of sample temperature for fixed oxygen pressures, using mass spectrometric detection of the desorbed species, as shown in Figure 7. The elemental B and La desorption from a clean surface are included for comparison. The relative yields of the various species have been determined by correcting for the mass spectrometer transmission variation with mass, and assuming that the ionization probabilities of B, B_2O_2 and B_2O_3 are the same and that La and LaO are the same. It is clear, if this assumption is correct, that the major species desorbing in the range $1000 < T < 1600$ K is B_2O_2.

The structure indicated in Figure 7 in the temperature range $1400 < T < 1600$ is echoed more strongly in Figure 8, where the temperature dependence of B_2O_2 removal is plotted for various oxygen pressures. Although the sharply peaked structure is present for all pressures above 1×10^{-7} torr, the peak positions appear to shift with increasing pressure to higher temperature. The precise cause of the highly reproducible structure is not understood, but the extreme sharpness of the structure may be the effect of some sort of resonance phenomenon in the reaction producing B_2O_2. It is interesting to note that in the same temperature range, the Auger data (Figure 9) show a marked increase in oxygen signal, a corresponding decrease in boron signal

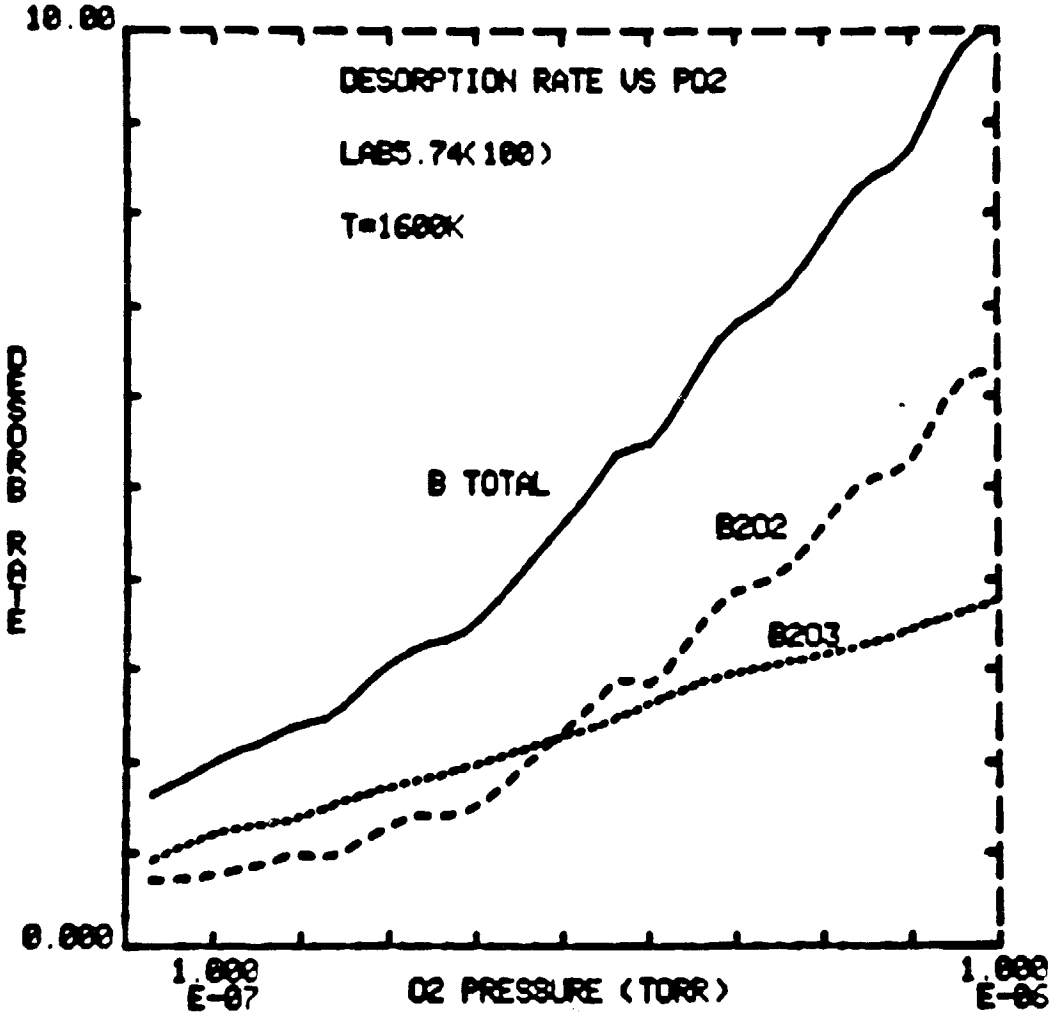

Figure 6. Desorption rate vs oxygen pressure for B_2O_2, B_2O_3 and total B from $LaB_{5.74}(100)$ at a sample temperature of 1600 K. Total B based upon assumptions discussed in text.

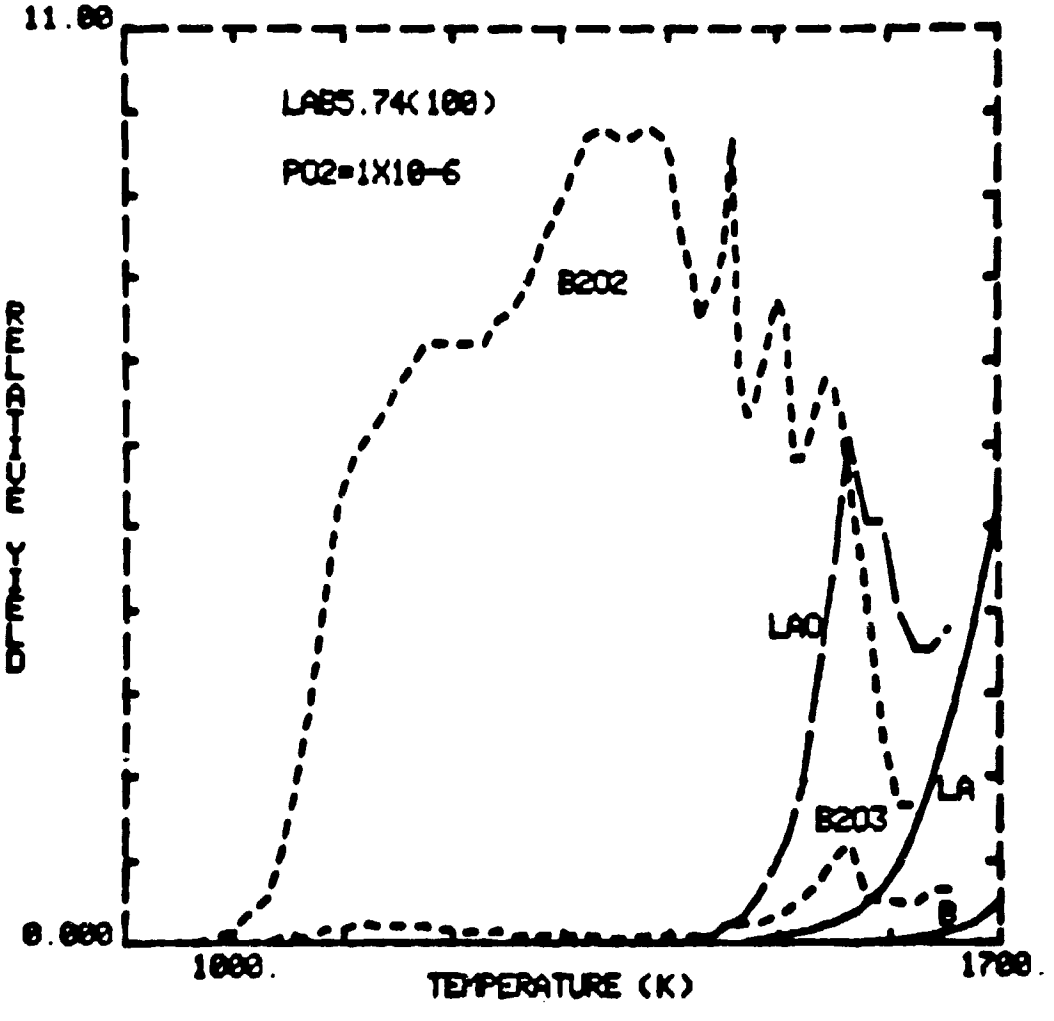

Figure 7. Relative desorption yields of B and La oxides from $LaB_{5.74}$ as functions of temperature in an oxygen pressure of 2×10^{-6} torr. Elemental La and B evaporation from the clean surface are included for comparison.

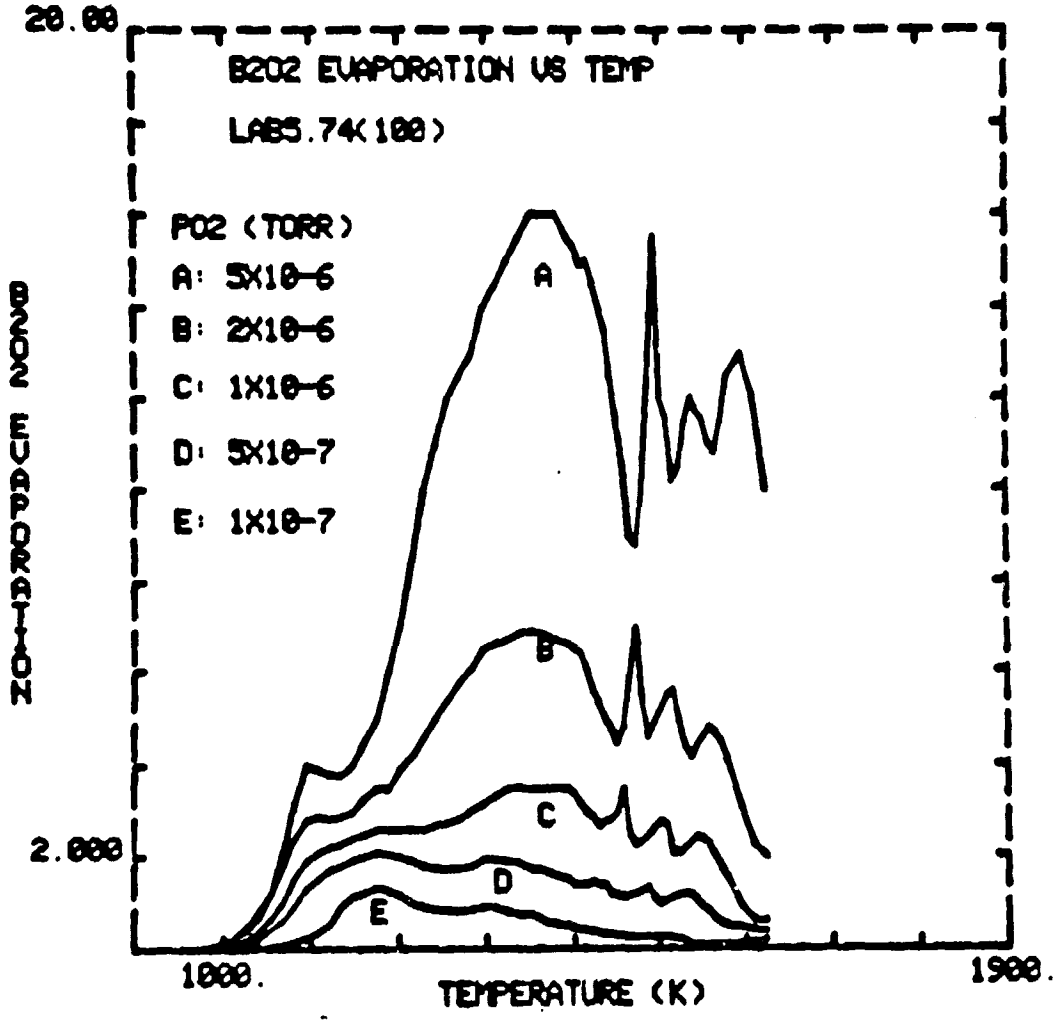

Figure 8. Variation with temperature of B_2O_2 evaporation rate from $LaB_{5.74}(100)$ in various fixed oxygen pressures.

and a slight increase in lanthanum signal. There is apparently a significant change in the surface layer in this temperature range.

The variations in boron, lanthanum and oxygen Auger signals from the surface have been studied under the same conditions, with results given in Figure 9. These results are similar to those of Bas, et al.,[9] who studied the surface concentrations of La, B and O on LaB_6(110) and (100) by Auger electron spectroscopy, during O_2 exposure at various temperatures. These authors also noted that extended heating in O_2 produced a grooved structure, {100} facets, on the (110) plane. The (100) plane was stable under this treatment, showing only steps of (100) orientation.

From a comparison of Figures 7 and 9, one may conclude that, at temperatures of about 1700 K, oxygen interaction ($P_{O_2} \lesssim 1 \times 10^{-6}$ torr) with the $LaB_{5.74}$(100) surface decreases to a negligible level, since no appreciable quantity of oxides is desorbing and no oxygen is bound to the surface. At this temperature, La becomes the dominant desorption product.

A final observation from the Auger data is the development of a satellite peak a few eV below the boron 179 eV peak when oxygen is present on the surface. For a given oxygen pressure, the boron peak shape changes with temperature. In Figure 10 the shapes of clean and oxygen-affected boron peaks are shown for various temperatures. In Figure 11 the variation of the boron satellite peak with temperature for a fixed oxygen pressure of 2×10^{-6} torr is plotted, using the

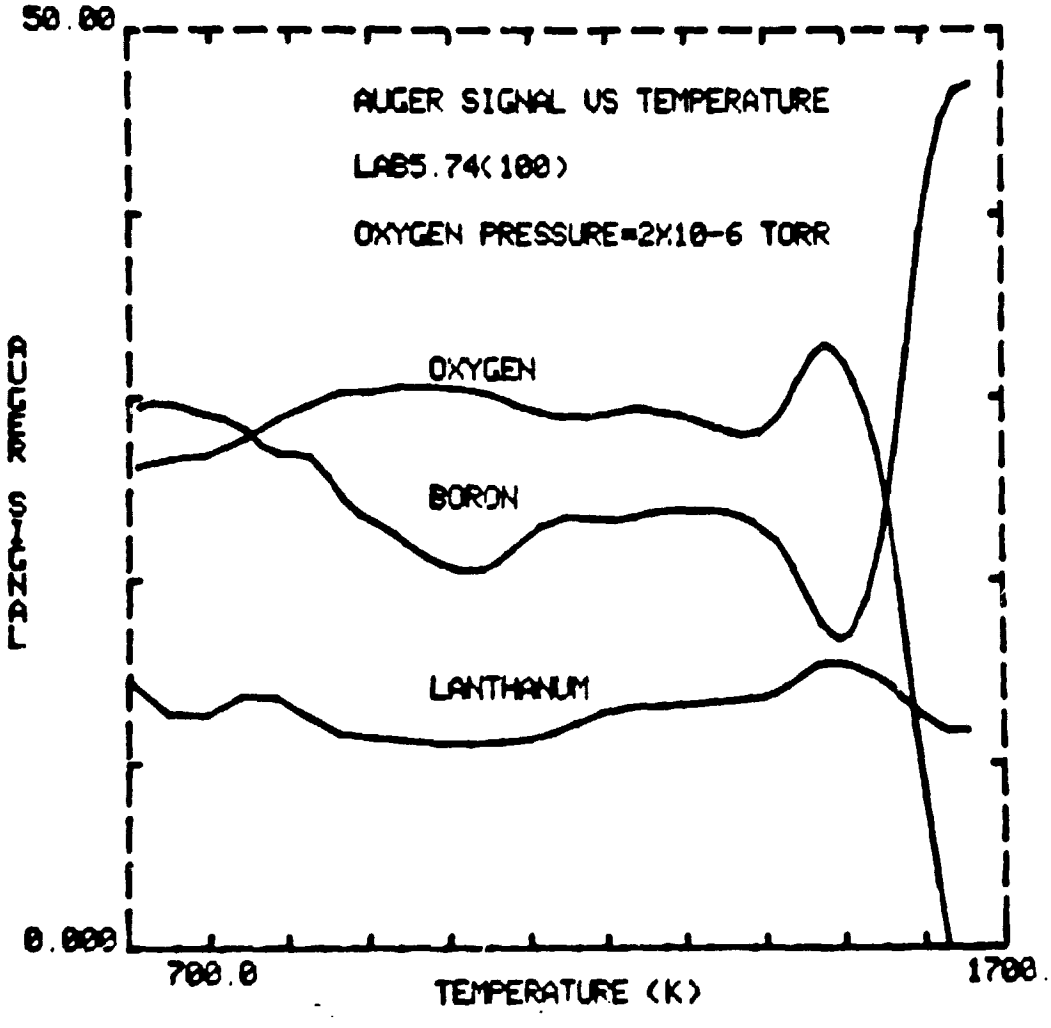

Figure 9. Variation of O, B and La Auger peak to peak amplitudes on $LaB_{5.74}(100)$ as functions of temperature in a fixed oxygen pressure of 2×10^{-6} torr.

amplitude difference between the top of the satellite and top of the main peak as a measure of the satellite peak height. The inflection points in this curve (maximum at ~ 1000 K, plateau at 1400-1500 K) may be correlated with, respectively, the onset of desorption of boron oxides and the region of sharp structure in the B_2O_2 spectrum (see Figure 7). Comparison with Figure 9 shows that the boron Auger signal has minima and the oxygen has maxima at both inflection points of Figure 11. It is apparent that the data presented here contain a wealth of chemical information about the $O_2/LaB_{5.74}(100)$ surface interaction. It is difficult, however, to interpret these results in light of the present limited understanding of the reaction mechanisms involved.

III. Fabrication and characterization of Zr/W and Hf/W alloys - Task B

Samples of bulk polycrystalline alloys were prepared by sintering, with compositions of W-5% Zr, W-1% Zr, W-.5% Zr, W-5% Hf, W-1% Hf and W-.5% Hf. The W-.5% Hf and W-5% Hf samples were studied in detail. These particular compositions were chosen initially for two reasons: 1) The Hf concentrations bracketed the total range available and 2) earlier field emission studies[4] had suggested that Hf should be at least as effective as Zr in lowering the surface work function.

Bulk properties of all but the W-1% Zr material were examined after interior surfaces had been exposed by cutting with a SiC abrasive wheel. Of the five samples examined, four (W-.5% Zr, W-.5% Hf, W-1% Hf and W-5% Hf) appeared uniform. Sections of these samples could be fractured with moderate force, but cutting with SiC abrasive

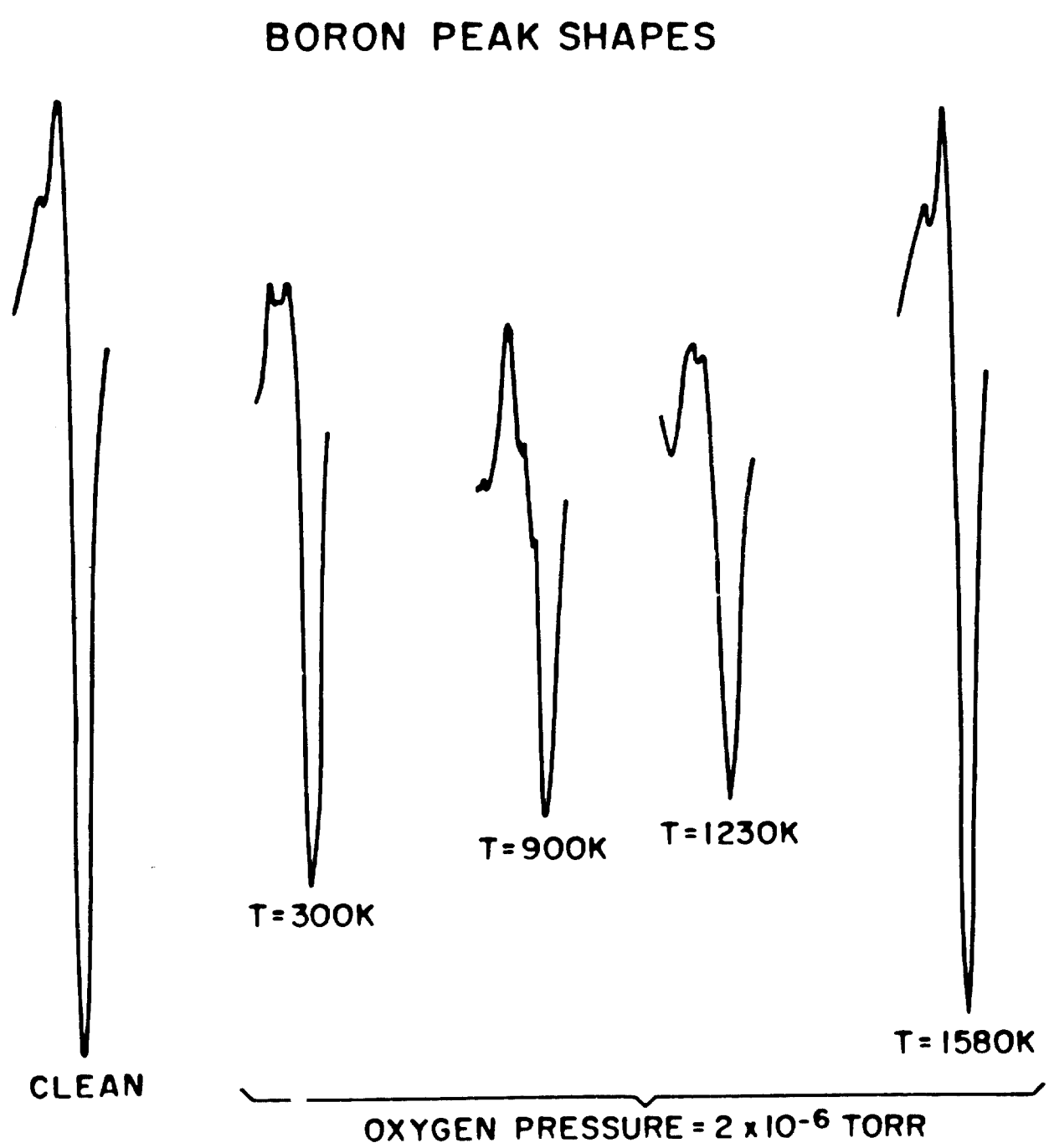

Figure 10. Change of boron Auger peak shapes with temperature at 2×10^{-6} torr oxygen pressure.

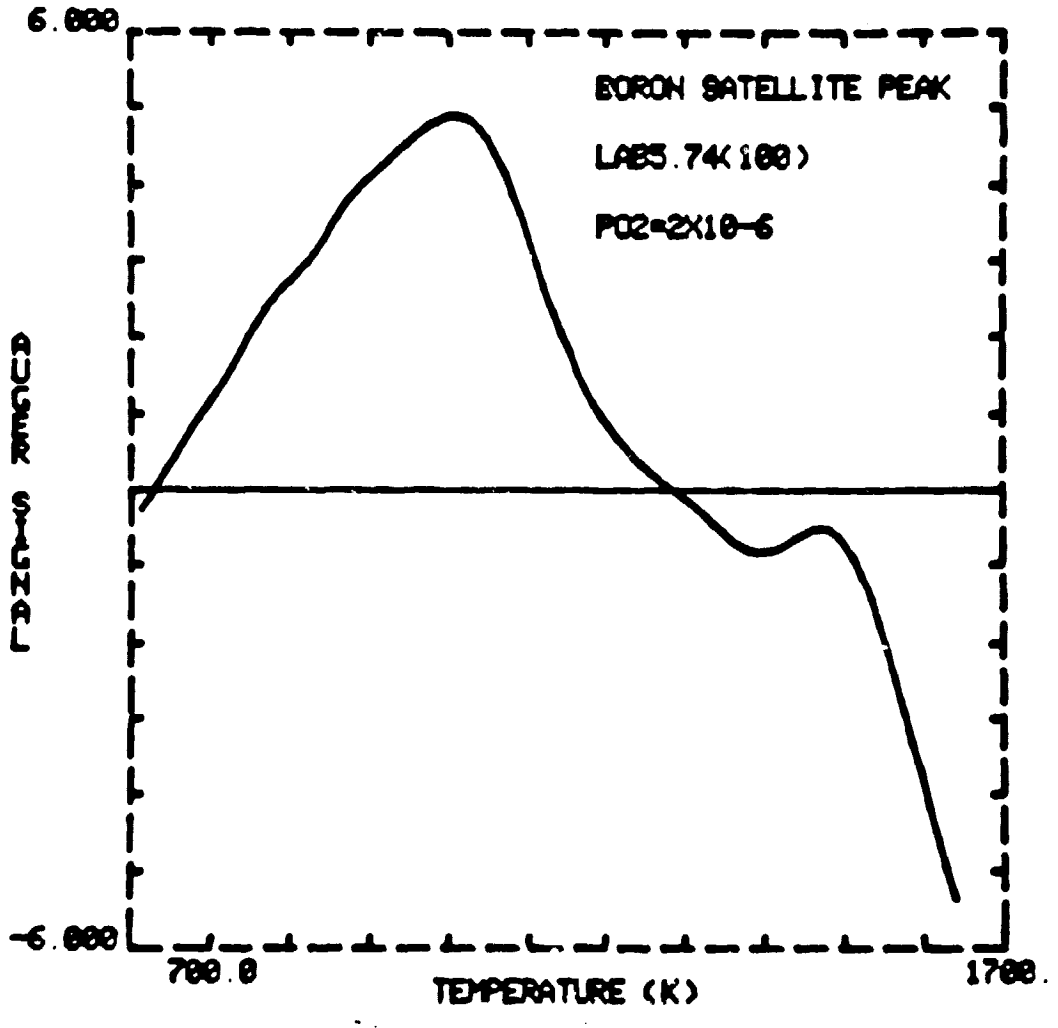

Figure 11. Change of B satellite peak amplitude as a function of temperature for $LaB_{5.74}(100)$ in an oxygen pressure of 2×10^{-6} torr.

was slow and tedious. The surfaces exposed by the cutting wheel were quite smooth, as observed by optical microscopy and low magnification scanning electron microscopy (SEM). The W-5% Zr sample, on the other hand, was porous and brittle, tending to crumble, with the exposed surfaces showing a large number of pits. The two sample surfaces to be investigated in detail were polished on successively finer grades of wet SiC paper, and finished on .3 μm alumina. The surfaces then showed mirror finishes, except for a high density of pits, particularly on the W-5% Hf sample. It was previously believed that these samples were of near-theoretical density, but that is apparently not true. The surfaces of the high-Hf sample especially was cold-worked during the initial cutting phase to the extent that voids in the material were obscured. These macroscopically damaged layers were removed during subsequent polishing steps, yielding smooth surfaces with pits.

Bulk compositional examination of the various alloys was done using x-ray energy dispersive electron microprobe analysis in conjunction with SEM. However, the resolution of this technique (~ 160 eV) was not sufficient to allow detection of 5% or less of Hf or Zr in a W matrix, for two reasons. First, the major Hf and Zr transitions are very close to those of W and second, the background bremsstrahlung radiation detected by the instrument is about 5% of the W signal amplitude in the region of interest.

The samples were then re-examined in the electron microprobe using a high resolution (~ 10 eV) wavelength spectrometer. In this case, the

narrow detection window allowed good separation between Zr and Hf peaks and W matrix peaks, and gave signal/noise ratios of 3 to 15 for all the samples examined. Because the measured intensities of the Zr and Hf peaks are somewhat dependent upon sample roughness and orientation in the microscope, the results of these measurements are only qualitative. However, it appeared that relative bulk concentrations of the minority elements in the alloys were approximately what had been expected from the ratios of Hf/W and Zr/W before sintering.

Initial analysis of the sample surfaces by AES showed approximately the bulk concentrations of W and Hf to be present, in addition to contamination. The surface concentration of Hf increased after heating, however, reaching levels much higher than those in the bulk. Results of the AES measurements are summarized in Tables VIII and IX. Some clarification of these results is necessary. In order to get precise measurements of the ratio of Hf to Hf + W (the value used in bulk characterization of the alloys), Hf(1624) and W(1736) Auger peaks, which have nearly the same electron escape depths, were used. It was necessary to use the high energy Hf transition in total surface composition determinations, because the low energy peaks for this element are overlapped by larger W peaks.

An interesting result, shown in Table IX, is the fact that appreciable Hf and O are present on the surface, even after significant evaporation has occurred. This result suggests rapid diffusion from the bulk to the surface by these elements, to replace desorbed material.

TABLE VIII

Summary of AES Results (W - .5% Hf)

Surface Concentrations of Elements[1]

Heat Treatment In Vacuum	$\frac{Hf(1624)}{Hf(1624) + W(1736)}$ (%)	% of Total Surface Composition						
		W(163-169)	Hf(1624)	C(272)	N(379)	O(503)	K(252)	Ca(291)
None	0	11	0	72	2	15	0	0
1050 K, 5 min	3	79	3	5	0	9	3	1
1163 K, 5 min	1	73	1	1	-	21	3	1
1335 K, 5 min	1	77	1	2	-	18	1	1
1465 K, 5 min	0	75	0	2	-	21	0	2
1610 K, 5 min	0	77	0	4	-	17	-	2
1685 K, 5 min	0	78	0	3	-	19	-	0
1910 K, 1 min	9	76	6	5[2]	-	13	-	-
2100 K, 30 sec	7	70	4	12[2]	-	14	-	-

(1) Corrected for elemental sensitivities according to Physical Electronics Industries Auger Handbook. Numbers in parentheses indicate energy of measured Auger transition

(2) Shows carbide Auger peak shape

TABLE IX

Summary of AES Results (W - 5% Hf)

Surface Concentrations of Elements[1]

Heat Treatment In Vacuum	$\frac{Hf(1624)}{Hf(1624) + W(1736)}$ (%)	% of Total Surface Composition								
		W(163-169)	Hf(1624)	C(272)	N(379)	O(503)	K(252)	Ca(291)	Si[2]	P(120)
None	5	24	3	50	2	18	-	3	-	-
1055 K, 5 min	4.5	72	3	7	0	17	1	0	-	-
1230 K, 5 min	5	72	3	1	0	22	2	0	-	-
1475 K, 5 min	7	59	5	9	0	18	-	6	3	-
1510 K, 2 min	22	55	10	11[3]	6	13	-	-	3	2
1625 K, 30 sec	22	53	11	8[3]	5	13	-	-	1	9
1730 K, 30 sec	22	59	11	6[3]	3	14	-	-	-	6
1850 K, 30 sec	24	57	12	10	5	16	-	-	-	-
> 2200 K[4]	16	70	10	4	-	16	-	-	-	-

(1) Corrected for elemental sensitivities according to Physical Electronics Industries Auger Handbook. Numbers in parentheses indicate energy of measured Auger transition.
(2) Si peak may shift from 92 eV to 76 eV upon formation of SiO_2. Observed peak here was 81 eV.
(3) Shows carbide Auger peak shape.
(4) Temperature exceeded 2200 K for a few seconds, due to increased electron emission from bombarding filament, caused by Hf evaporation onto that filament.

It appears that O is present in the bulk, and is not merely a surface contaminant.

Thermionic and FERP work function measurements were made on the W-.5% Hf and W-5% Hf alloy samples. These experiments were performed after heating the samples to T = 2100 K for short times. A summary of results is given in Table X, where ϕ_R = Richardson work function, A_R = Richardson pre-exponential factor and FERP 10%-90% is a measure of width of the derivative FERP collected current curve. A discussion of FERP and thermionic work function measurements on polycrystalline surfaces is in order, to clarify the results shown in Table X.

TABLE X

Sample[1]	ϕ_R (eV)	A_R (A-cm^{-2}-K^{-2})	ϕ_{FERP}[2] (eV)	FERP 10%-90% (meV)
W-.5% Hf	2.65	.016	5.5[3] (4.5)	510[3] (360)
W-5% Hf	3.27	2.0	3.88	300

(1) After heating to 2100 K for ~ 10 sec.

(2) Because the measured distributions (FERP 10%-90% values) were much wider than the true emitted electron energy distribution, the uncorrected peak position of the differential curve of collected current was used as ϕ_{FERP}.

(3) Numbers in parentheses indicate stable values after > 60 sec total heating at 2100 K. The W-5% sample showed no changes after the initial ~ 10 sec heating.

A polycrystalline sample may have many different crystal planes exposed at its surface, particularly when the sample has not been subjected to any special mechanical treatment. It is well known that drawing or rolling polycrystalline materials causes preferred surface orientations to develop. In addition, long-term heating may induce growth of particular crystal planes at the expense of others because of surface energy considerations. In the present case, however, polycrystalline samples were cut from the bulk of sintered alloy material and polished, so a random assortment of exposed surface planes was expected.

In general, different crystal planes of a pure metal have different work functions, due to bulk and surface electronic effects. In addition, binding characteristics of a given adsorbate on different planes are different, because of surface geometric and electronic properties. Finally, the work function change with coverage of a given adsorbate varies from plane to plane. We may therefore represent the surface of a W-Hf alloy (with some oxygen present, as previously observed) as an array of patches of different crystal orientation, each with a particular Hf and O coverage and each with a different work function.

The work function analysis of patchy surfaces is difficult, with measured values being some kind of average. Because the sizes and distributions of the various work function patches are not known, the meaning of "average" is not clear. However, from the practical point of view, polycrystalline materials are easy to fabricate in

comparison with single crystals and therefore may have greater technological importance. We have therefore used both FERP and thermionic techniques to get two different "average" work function measurements for each surface, the comparison of which will now be discussed.

The FERP technique provides two results, the work function (ϕ_{FERP}) and apparent energy distribution of collected electrons characterized by the 10%-90% value of the differential curve. To a first approximation, ϕ_{FERP} may be considered a true geometric average such that

$$\phi_{FERP} = \frac{1}{\Sigma S_i} \sum_j S_j \phi_j \qquad (1)$$

where S_j and ϕ_j correspond to the surface area and work function of the j^{th} patch. This average may be strongly distorted, however, if adjacent patches differ much in work function. In that case, very high local fields may be sustained which would upset the purely geometrical average. The FERP 10%-90% value gives a qualitative idea of the range of variation of patch work functions, larger values indicating larger variations. For the analyzer used here, a single crystal surface would be expected to show a 10%-90% value of 160 meV or less.

Thermionic measurements, on the other hand, yield an "average" which is strongly weighted toward low work function. For patches of surface area S_j and work function ϕ_j, the Richardson equation may be written (neglecting local patch-induced fields and reflection effects)

$$J = \frac{I}{S} = \frac{\sum_i I_i}{\sum_j S_j} = \frac{\sum_i S_i A T^2 \exp(-\phi_i/kT)}{\sum_j S_j} \qquad (2)$$

where J is the total current density and A is the Richardson constant, 120 A-cm^{-2}-K^{-2}. Because of the exponential dependence on ϕ in Eq.(2), terms involving small ϕ_i (low work function patches) would be expected to dominate, even if the corresponding S_i were small. Thus, a surface with a small area of very low work function patches and a high area of high work function patches would yield a low Richardson work function and low pre-exponential term. On the other hand, the geometrical weighting of the FERP results would give a high ϕ_{FERP} and 10%-90% value depending on the relative areas of the different work function patches. Again, this analysis neglects the effects of local patch fields, which could strongly distort the weighted work function averages.

The values of ϕ_R and ϕ_{FERP} given in Table X are not inconsistent with the above discussion. It is clear that each alloy surface has patches of different work function, although the effect is more pronounced on the W-.5% Hf sample. It is likely that the Hf coverage on the W-5% Hf sample is approaching one monolayer, in which case the work functions of all planes would tend to converge to the bulk polycrystalline Hf value (~ 3.5-4.0 eV). Thus, there is little discrepancy between ϕ_R and ϕ_{FERP} values for this sample. The W-.5% Hf sample, on the other hand, shows a larger discrepancy, higher FERP 10%-90% value and lower ϕ_R confirming the presence of lower work function patches.

In addition, the data obtained for the W-.5% Hf sample showed much more sensitivity to temperature cycling, probably indicating that Hf coverage was in a range where small desorption and diffusion effects could significantly alter the work functions of some patches.

Previous experience with Zr or Hf on W field emitters has shown that an activation with O_2 is necessary to achieve minimum work function. Studies of Zr and O_2 coadsorption on W(100) single crystal surfaces (conducted concurrently with the alloy studies, and to be discussed later in this section) indicated that oxygen-assisted diffusion of Zr into the substrate was an important step in the activation process. We therefore investigated the effects of equilibrium oxygen pressures on surface composition and emission properties of the W-5% Hf alloy at elevated temperatures. Table XI shows the changes in surface composition (ratios of Auger peak-to-peak amplitudes) of this sample during heating at 1538 K in oxygen. The effect is similar to that observed during heating in oxygen of Zr layers adsorbed on W(100), to be discussed later. However, in the present case the bulk concentration of Hf is 5%, a larger value than the Zr/W(100) case, so the effect is even more striking.

The results shown in Table XI are consistent with the mechanism proposed for the Zr/W case, that oxygen enhances Zr or Hf diffussion into the bulk, with subsequent formation of a tungsten oxide surface layer. However, in the case of polycrystalline alloys, there are more

possible diffusion mechanisms (e.g., along grain boundaries) so the comparison between the two cases must be done cautiously. Studies of Hf diffusion into W single crystals should allow a more direct comparison.

TABLE XI

Fffect of heating in oxygen on the surface concentrations of elements[1] in a W-5% Hf alloy

Treatment	Cumulative O_2 exposure (Langmuirs[2])	Hf(1624) / W(1736) (3) (4)	O(510) / Hf(1624)
30 sec, 2100 K in vacuum	0	.15	2.4
5 min, 1×10^{-7} torr oxygen, 1538 K	30	.13	3.9
+ 15 min, 1×10^{-7} torr oxygen, 1538 K	120	.08	5.0
+ 15 min, 5×10^{-7} torr oxygen, 1538 K	570	.02	13

(1) Auger peak-peak ratios, measured after cooling to 300 K
(2) 1 L = 1×10^{-6} torr-sec
(3) Auger electron energies, in eV, are given in parentheses
(4) W(1736) peak-peak amplitude stable within about ± 5% throughout

Subsequent heating in vacuum after the above oxygen treatments yielded results summarized in Table XII. After an initial heating period of about 3 min at 1450 K, the O/Hf ratio is essentially constant, even though the amount of Hf on the surface is increasing. That is, Hf and O diffuse to the surface together. The same effect was observed for the Zr/O/W(100) system.[5]

TABLE XII

Effect of heating in vacuum on the surface concentrations of elements[1] in a W-5% Hf alloy previously heated in oxygen

Total heating time at 1450 K	$\frac{Hf(1624)}{W(1736)}$[2]	$\frac{O(510)}{Hf(1624)}$	
0	.02	13	
1/2 min	.02	7.7	
1-1/2 min	.02	11	
3 min	.04	6.0	
6 min	.06	5.6	
12 min	.12	4.3	(3)
22 min	.12	5.5	
42 min	.14	5.0	

(1) Auger peak-peak ratios, measured after cooling to 300 K
(2) Auger electron energies, in eV, are given in parentheses
(3) Mean of last four values is 5.1, with standard deviation of .6

In a companion set of experiments, the effects of an oxygen partial pressure on the thermionic emission properties of W-.5% Hf and W-5% Hf alloys were studied. The emitted current densities at various applied voltages were measured for constant temperature of each alloy, as functions of oxygen pressure. However, because of adsorption and subsequent electron stimulated desorption of oxygen from the collector surface quantitative determinations could not be made. The qualitative result was that the W-.5% Hf alloy, after a 2100 K flash, showed a

monotonic decrease in thermionic emitted current at 1550 K during an oxygen exposure of 1×10^{-8} torr, whereas the flashed W-5% Hf alloy showed an initial current increase during the same treatment at 1×10^{-8} or 1×10^{-7} torr, followed by a decrease in emitted current at longer exposure time at the higher pressure.

These results suggest that the Hf coverage on the W-.5% Hf alloy surface, after heating to 2100 K, is equal to or less than that yielding a minimum work function and decreases with oxygen exposure, giving a higher work function. The W-5% Hf alloy, however, has a surplus of Hf after the 2100 K flash, and as the Hf coverage is decreased during oxygen exposure, the surface work function passes through a minimum before finally increasing.

As alluded to briefly in the preceding discussion, investigations of single crystal surfaces were also conducted. These studies are very important since, in general, only single crystal surfaces are homogeneous enough, with respect to both geometry and electronic properties, to allow detailed analysis of the surface processes involved. For example, diffusion from bulk to surface in a polycrystalline sample may involve primarily diffusion along grain boundaries, whereas this path is not present in single crystals. Additionally, the patch work function problems discussed previously do not appear on single crystal surfaces. We therefore conducted a detailed, basic study of the coadsorption of zirconium and oxygen on a tungsten (100) single crystal surface. The results have been published in the scientific literature.[5] Therefore,

only a summary of the pertinent results of that work will be discussed here.

The Zr/O/W(100) system provides a rare example of a low work function (2.6 eV) surface stable over a wide temperature range, 300 to 1800 K. It has been established that heating a Zr-covered W(100) surface in oxygen promotes rapid diffusion of Zr and O into the bulk along with the formation of a residual tungsten oxide layer. Subsequent heating in vacuum causes a remarkable work function drop, from 5.5 eV to 2.7 eV (nearly 3 eV!) after heating at 2100 K for 10 sec.

Thermal cycling in oxygen and in vacuum after an initial several monolayer dose of zirconium is the most reliable way to obtain the low work function, but it is also possible to obtain it by an initial oxygen dose followed by a zirconium deposition. A typical sequence involves a 10^{-5} torr-sec oxygen dose at 1000 K, one minute anneal at 1200 K, and a few monolayer zirconium deposition at 1000 K. Subsequent one minute heating steps up to 1700 K produced a 1.4 eV drop in the work function, with only a very small change in the composition of the surface. Apparently an activation energy exists for formation of the low work function surface, and thermal heating to 1700 K is required to overcome this energy barrier.

Although oxygen is necessary for achieving the low work function surface, a partial pressure of oxygen can destroy the thermionic emitting properties of the surface by motivating the diffusion of the Zr-O complex away from the surface. However, subsequent heating in vacuum

will restore the low work function surface through bulk diffusion of the Zr-O complex to the surface. This is an unusual example of a low volatility dispenser type thermionic cathode where the matrix is a single crystal.

The specificity of the Zr-O complex for enhanced work function lowering of the W(100) crystal is believed to be caused by geometric considerations which allow the Zr-O complex to be densely packed and configured so as to contribute its maximum dipole moment to the reduction of the surface potential. The unusual thermal stability of the low work function surface is evidence that the adsorption sites for the Zr-O complex on the W(100) surface possess a large binding energy which cause localized adsorption to occur throughout a wide temperature range.

Field emission noise measurements show that surface mobility occurs for $T \gtrsim 1000$ K,[22] yet it is remarkable that this composite surface layer retains its ability to maintain a low work function on the W(100) surface at even much higher temperatures (e.g. ~ 2100 K). The extremely high temperature (T ~ 2400 K) required to rid the surface of traces of zirconium after a several monolayer dose is due both to the low volatility of the Zr-O complex (as determined by the lack of volatile desorption products) and bulk solubility of the Zr-O complex.

Careful examination of the desorption products by a quadrupole mass spectrometer (QMS) placed 5 mm from the W(100) crystal with various amounts of coadsorbed zirconium and oxygen showed no evaporating

species of Zr, ZrO or ZrO_2 when heated to 1600 K in vacuum or in the presence of oxygen at 10^{-7} pressure. The sensitivity limit of the QMS was ~ 10^{-12} torr. On the other hand, adsorbed multilayers of zirconium on W(100) without coadsorbed oxygen can be quantitatively desorbed between 1500 and 1900 K.[23] Further evidence of the enhanced stability with respect to desorption of the coadsorbed layer is given by the fact that long term heat treatments at $T \gtrsim 1700$ K caused no change in the surface work function.

The work function for Zr/O/W(100) has been determined two ways: ϕ (FERP) = 2.65 ± .05 eV, and ϕ (Richardson) = 2.56 ± .05 eV with a pre-exponential $A_R = 6 \pm 2$. The fact that the pre-exponential differs from the theoretical value of 120 implies a temperature dependence of the work function or a large reflection coefficient.

Carbon impurities apparently lower the work function while the presence of nitrogen can increase the work function to almost 4 eV. The nitrogen cannot be removed by heating in vacuum at 1800 K, but can be removed by heating in oxygen at ~ 1600 K. This suggests formation of the stable nitride ZrN and subsequent removal by oxidation to NO or NO_2. On the other hand, heating in CO followed by moderate heating to 1700 K appears to be just as effective in obtaining the low work function surface as the standard heating in oxygen followed by a 2100 K flash.

Current densities of > .1 A/cm^2 have been obtained for T > 1600 K, although outgassing of the support leads prevented systematic measurements at this temperature. Extrapolation to 1800 K predicts a thermionic emission density of 2.2 A/cm^2.

Examination of the LEED patterns both before and after Richardson measurements of the low work function Zr/O/W(100) surface revealed predominantly a (1 × 1) pattern. Higher temperature annealing occasionally produced the $\left(\frac{4}{3} \times 2\right)$ pattern reported by Hill, et al.,[24] with supposedly oxygen-free zirconium adsorption. Thus, from the LEED studies we can associate the (1 × 1) pattern with the low work function Zr/O/W(100) surface, although we cannot rule out the occasional occurrence of a more complex overlayer than (1 × 1) with the low work function surface.

The low work function associated with the Zr/O/W(100) surface has not been observed on other W planes, although similar results have been noted for Zr/O/Mo(100) and Hf/O/W(100).[4] Hafnium and zirconium have nearly identical chemical behavior, as do tungsten and molybdenum, and tungsten and molybdenum have almost identical lattice spacing. One may rule out bulk factors such as the alloying of the Zr-O complex as cause for the low work function, since a shift in the bulk Fermi level would affect all crystal faces equally which is clearly not the case. Thus, we conclude that geometric structure factors unique to the (100) plane provide the basis for the localized work function lowering by the Zr-O complex.

IV. Characterization of cesiated surfaces of promising electrode materials - Task C

A Shelton triode tube was built and tested. Such a device had been used in other studies[25-27] to measure retarding potential surface work functions and reflection coefficients of single crystal and polycrystal

pure metals and alloys in vacuum. Our goal was to use this technology to study work functions of LaB_6 and other promising emitter and collector materials under conditions of equilibrium cesium vapor. For several reasons to be discussed later however, the triode method is difficult to use in the study of low work function materials.

The triode was built with plane parallel geometry, and consisted of emitter and collector, whose roles could be interchanged, with an intermediate, apertured anode, which could be biased to overcome space charge. The entire electrode assembly was immersed in a near-uniform axial magnetic field of approximately 1000 gauss. The electrode spacing and aperture size were optimized to allow normal energy distributions of emitted electrons to be measured. Each electrode could be independently heated and biased so that independent Richardson measurements or contact potential difference measurements could be made.

The triode was set up with (110) and (100) oriented $LaB_{5.74}$ crystals as electrodes, and a Mo anode. Tests were made under vacuum conditions and several problems were encountered, as summarized in Table XIII. The difficulties can be divided into three categories: electrode contamination, electrode mounting problems and back emission. In previous work of this type[27] these problems were not observed, because high work function metallic electrodes were used, and the triode could be immersed in liquid nitrogen to prevent overheating and aid in maintaining low pressure. With LaB_6 electrodes, however, sample mounting stability is a serious problem, because the material is difficult to maintain contact with and because its high emissivity requires relatively high power

TABLE XIII

Summary of Major Problems Encountered with Shelton Triode During Vacuum Testing

Problem	Symptoms	Possible Solutions
Samples moved during heating (no longer parallel)	Broad knee in lnI vs. V plot (broadened energy distribution)	Heavier support leads
Photoemission from collector	Electron emission from collector in deep retarding region with emitter hot	Characteristic of low work function surfaces
Wall charging problems	Erratic measurements at low current; noise	Conductive coating on tube wall
Electron optical effects (beam focussing)	Extreme variation of collected current with anode potential Unreasonable lnI vs. V slope	Larger samples and closer spacing to anode
Loss of thermal contact to samples	Inconsistent sample heating, possible variation of emitter potential with temperature	Improved sample mounting method
Sample contamination due to tube outgassing	Rapid shift in apparent collector work function Unusually high emitter work function	Outgas all tube elements thoroughly
Overheating of anode during outgassing	Mo evaporation onto emitter and collector	Outgas at lower power

input for the necessary heating. Since the triode was to be used with an equilibrium cesium vapor, it could not be cooled; rather, additional heating was required. Therefore contamination was difficult to control. Finally, photoemission from the low work function collector could not be eliminated because of the close proximity of the hot emitter. Because of these difficulties, it was not possible to achieve proper operation of the Shelton triode tube for the electrode materials to be studied, even under vacuum conditions. It was therefore decided that this part of the project should be shelved in favor of nonequilibrium cesium measurements.

Nonequilibrium measurements of the effects of cesium adsorption on the work function of the $LaB_{5.74}(100)$ surface, both clean and oxygen covered, were made using the FERP technique. In addition, thermal desorption studies were performed to determine cesium binding energies on the surface. Comparison of these results yields information relevant to thermionic converter applications. Although not as direct as measured in an equilibrium cesium pressure, the nonequilibrium method allows more experimental flexibility and provides insight into the basic surface processes involved.

Figure 12 shows the variation of work function with cesium coverage on the clean $LaB_{5.74}(100)$ surface. Monolayer coverage was taken to be saturation in the Auger signal vs dose and the coverage indicated in Figure 12 is therefore the Auger signal normalized to its maximum value. The Cs Auger signal is indeed a linear function of the total quantity

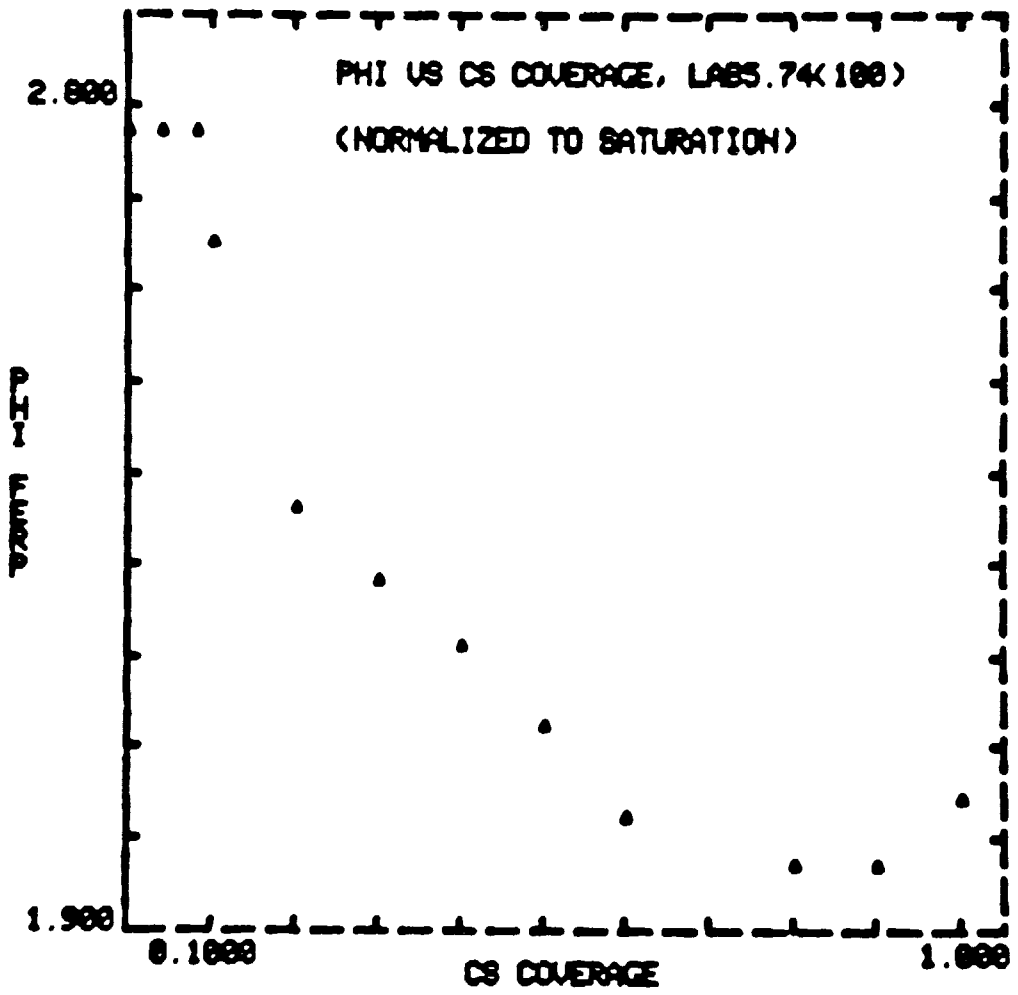

Figure 12. Work function vs coverage for Cs adsorption on clean $LaB_{5.74}(100)$.

of Cs adsorbed as indicated in Figure 13, where area under the Cs desorption curve is used as a measure of initial Cs coverage.

An interesting feature of the work function behavior with coverage is the initial plateau in ϕ as cesium is adsorbed. This reproducible effect has been observed only on LaB_6 crystals[8] and not on smooth metal surfaces. The initial, decreasing slope of a ϕ versus coverage curve is taken to be proportional to the surface dipole moment for cesium coverage approaching zero. Thus, the results of Figure 12 would seem to indicate zero initial dipole moment for cesium on $LaB_{5.74}$ (100). We believe, however, that surface roughness must also be considered in the case of LaB_6. Scanning electron micrographs of the surfaces studied here, and those used in other work,[8] show significant deviation from atomic smoothness. The (100) surface, in particular, has square depressions with dimensions 1-10 μm, presumably caused by thermal and/or oxygen facetting. Similar structure was observed on the (110) and (321) surfaces.

A possible explanation for the delayed work function decrease with cesium coverage thus would be that the cesium atoms, mobile on the surface at the 300 K adsorption temperature, preferentially adsorb within the depressions (at step edges, for example). It is likely that the low energy FERP electrons are primarily collected at the protruding steps of the surface rather than within the depressions. Thus, the initial fraction of a cesium monolayer would not cause a detectable change in the FERP I-V characteristics. The incident Auger beam and the

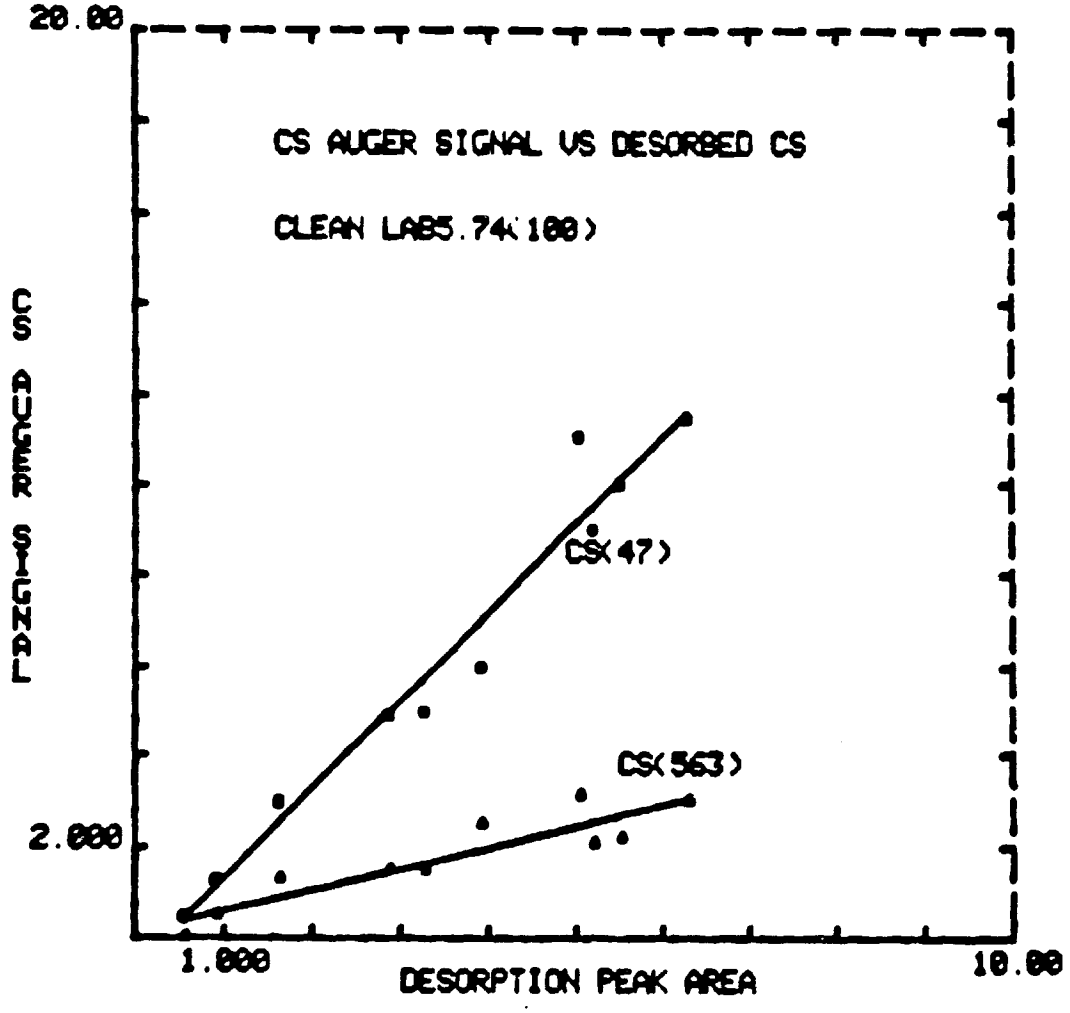

Figure 13. Auger signal vs coverage, determined by thermal desorption, for Cs on $LaB_{5.74}(100)$.

resulting Auger electrons, on the other hand, would be affected only slightly by the surface structure, yielding an initially constant measured work function with increasing cesium coverage.

A similar effect observed for oxygen adsorption on $LaB_6(110)$ could be explained in the same way: preferential adsorption at sites within surface depressions would be initially undetected by FERP measurements. Preferential adsorption within surface depressions would tend to increase surface roughness with prolonged oxygen exposure at elevated temperature by removal of oxide species, an effect which has been observed.[9]

The adsorption of Cs on oxygen-covered $LaB_{5.74}(100)$ surfaces results in work function changes indicated in Figure 14. Again, work function is plotted versus cesium Auger signal, normalized to saturation. The preadsorbed oxygen coverages are calculated in a similar manner. The minimum work function attainable under the adsorption conditions used here (both oxygen and cesium adsorbed at room temperature) was about 1.3 eV. No work function measurements were performed on oxygen layers heated above room temperature.

Desorption of neutral cesium from saturated cesium layers on clean $LaB_{5.74}$ and from .7 monolayer oxygen-covered surfaces, both thermally equilibrated and non-equilibrated, yielded data shown in Figure 15. In both cases with adsorbed oxygen, cesium desorption is shifted to higher temperature (higher binding energy) as expected. The thermally equilibrated case was achieved by saturating the clean surface with oxygen, heating to 1400 K and cooling the sample. After

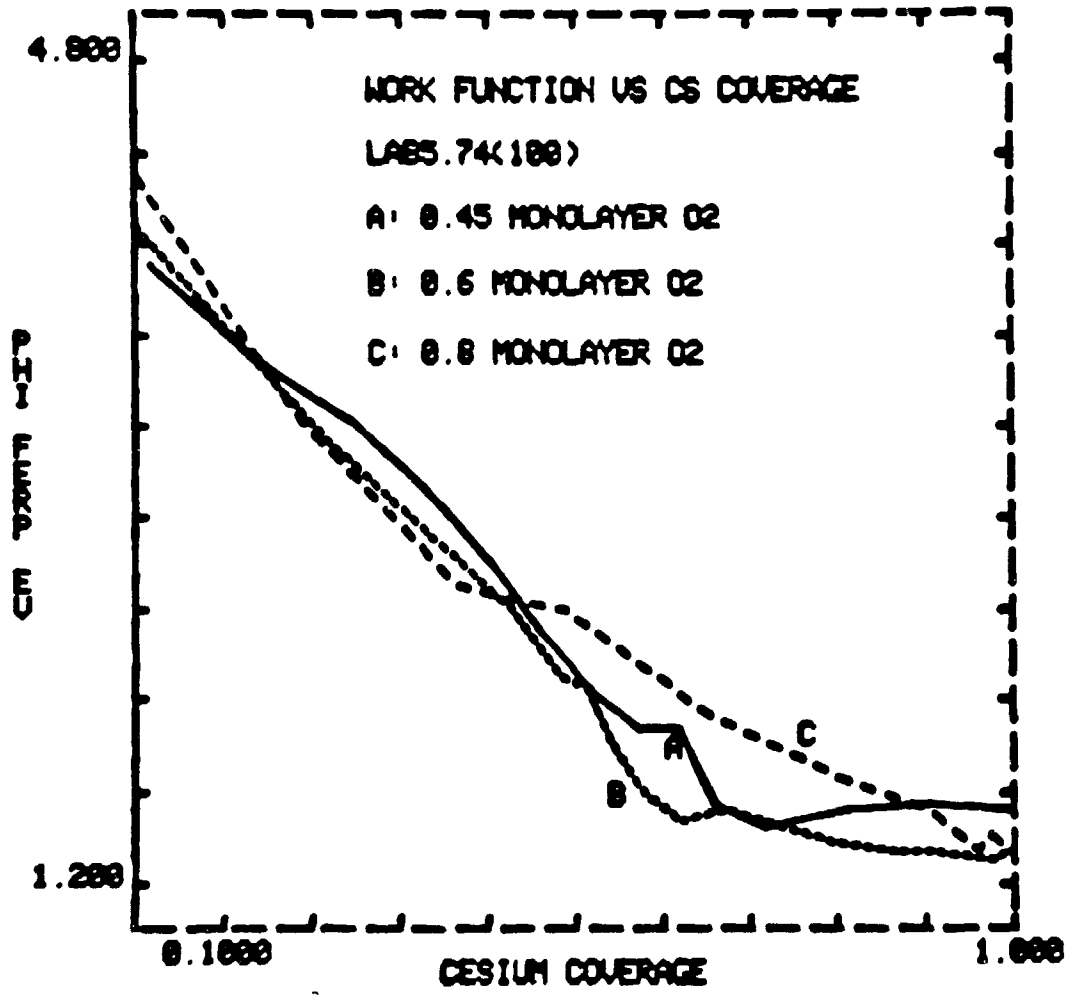

Figure 14. Work function vs cesium coverage for various oxygen coverages on $LaB_{5.74}(100)$.

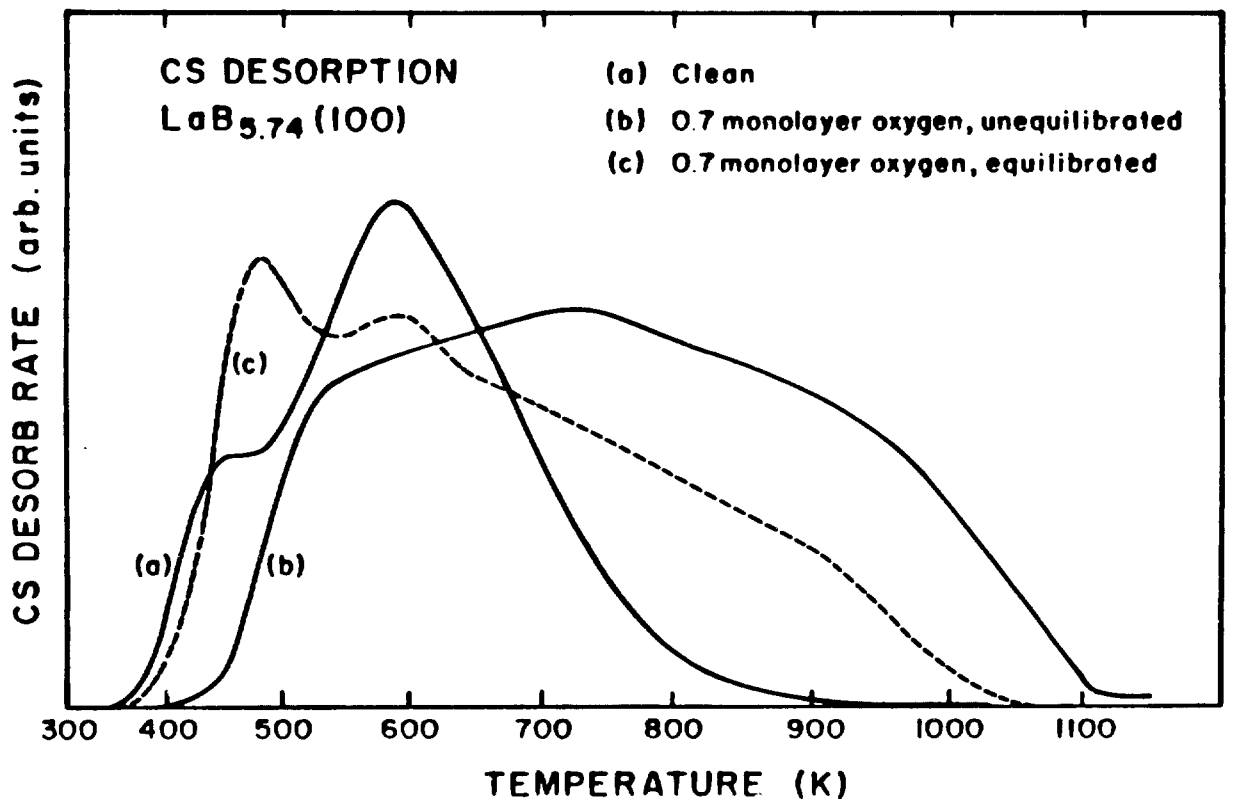

Figure 15. Cs desorption from $LaB_{5.74}$(100) surfaces. a) clean; b) 0.7 monolayer oxygen, unequilibrated; c) 0.7 monolayer oxygen, equilibrated at 1400 K.

this treatment, only .7 monolayers of oxygen remained, as determined by AES. Thus, as discussed under Task B, a significant quantity of boron oxides had been desorbed from the surface. This effect apparently reduces the overall affinity of the surface for cesium as compared with the case of a non-equilibrated oxygen layer. On the other hand, the nearly featureless spectrum obtained from the non-equilibrated oxygen layer suggests that, in this case, no well defined binding sites exist, although cesium is more difficult to desorb. It is likely that thermal equilibration effectively causes oxygen to bind more tightly to the surface (primarily covalent bonding) leaving fewer oxygen electrons available for ionic Cs-O bonds.

The adsorption of cesium on the W-.5% Hf and W-5% Hf alloys previously discussed was studied briefly by FERP. The surfaces were initially heated to ~ 2100 K and cooled to room temperature, yielding average FERP work functions of 4.5 and 3.9 eV, respectively. Cesium was then adsorbed in small doses from the well-outgassed, high-purity cesium source. Before each dose, the source was allowed to stabilize at a constant cesium evaporation rate, so that the total amount of cesium deposited was proportional to the dosing time. Under these conditions one would expect to observe cesium coverages up to one monolayer, but multilayer growth should not occur because of surface diffusion and reevaporation of cesium from the surface. Multilayer growth would be expected only at reduced temperatures.

The results of the cesium adsorption experiments are shown in Figure 16, with work function minima of 1.65 and 1.85 eV for W-.5%

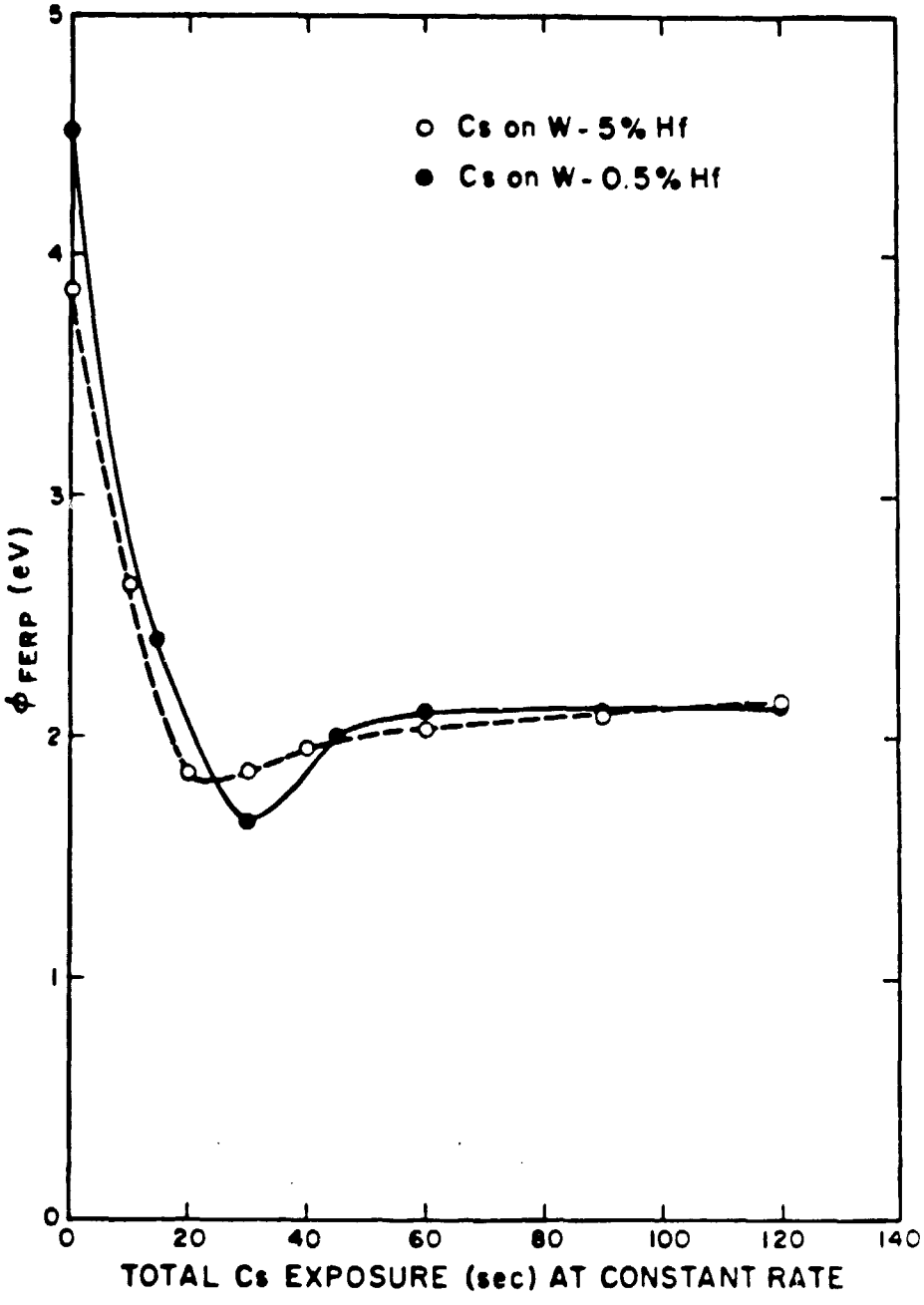

Figure 16. Work function variation with Cs exposure of W-Hf alloy surfaces

Hf and W-5% Hf substrates, respectively. It should be pointed out that, since the FERP method measures a geometrically averaged work function, the values observed probably are not indicative of those which would be measured for the most favorable planes of the surfaces. These results might be altered significantly by coadsorption of oxygen and cesium, although such experiments have not yet been done.

It is interesting, however, that even for the complicated surfaces of the alloys, cesium adsorption produces work function behavior similar to that observed for most clean, pure metal surfaces, that is, with increasing coverage the work function drops rapidly to a minimum (at about 1/2 cesium monolayer) and then rises to a steady value corresponding to the work function of bulk cesium. Also, the surface with higher average initial work function yields the lower minimum value, an observation which has been made for many other systems.

Because of the mounting system used for the W-Hf alloy samples in these studies, temperatures below 1000 K could not be measured. Therefore, cesium thermal desorption experiments would have provided little useful information, since most of the desorption occurs below 1000 K.

The adsorption of cesium on the low work function Zr/O/W(100) single crystal surface was investigated in more detail. As in the $LaB_{5.74}$(100) work, the techniques of AES, FERP and thermal desorption spectroscopy were used for surface characterization. In Figure 17 the change in cesium Auger signal (563 eV peak) is shown as a function

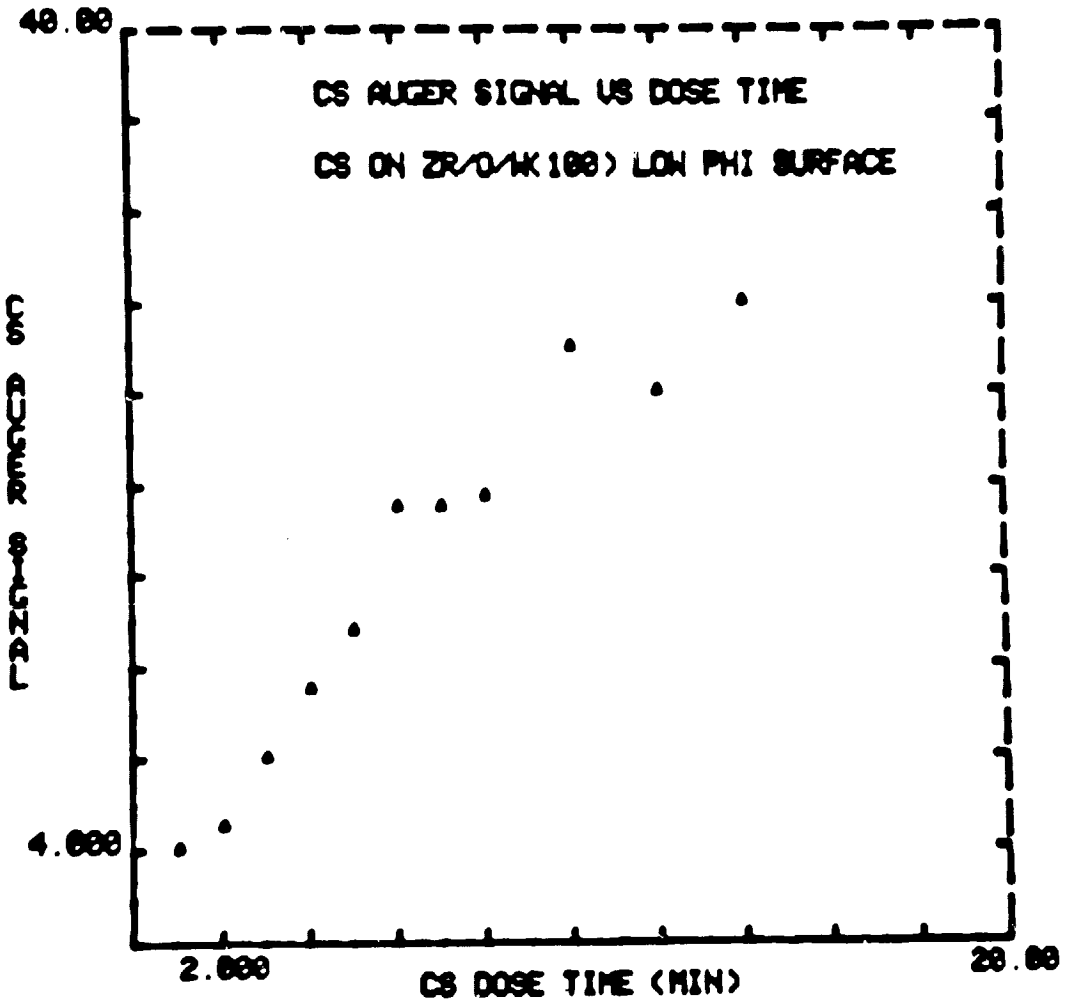

Figure 17. Increase of Cs Auger signal with dose time on Zr/O/W(100) surface. Above 8 min, the cesium/oxygen ratio is approximately constant.

of dose time. During the time of these measurements, a slight problem with system contamination was encountered, corresponding to a background oxygen pressure of 1×10^{-10} torr or less. The plateau in Figure 17 at about 6 min cesium dose time is believed to correspond to saturation of the initially clean surface, while the additional adsorption beyond 3 min is attributed to oxygen/cesium coadsorption. At times greater than about 8 min, the surface Cs/O_2 ratio was determined by Auger to be approximately constant, in support of the above explanation. Adsorption of cesium to greater than monolayer coverage in the presence of oxygen has also been observed by Desplat on W(110).[28]

The change in work function corresponding to adsorption as in Figure 17 is shown in Figure 18. Because of the uncertainty in monolayer assignment, the dose scale has not been converted to coverage. The minimum work function attained was about 1.9 eV and apparently corresponded to near saturation cesium coverage. Note that the terminal value of ϕ dropped to ~ 1.7 eV after additional oxygen had adsorbed from the background gas.

After the system background problems were remedied, a series of desorption experiments was performed. Figure 19, curves A and B show the effect of heating on saturated Cs layers on clean and oxygenated Zr/O/W(100) surfaces, respectively. In this context, clean means the flashed (2100 K) Zr/O/W surface with $\phi \leq 2.8$ eV, while oxygenated means the clean surface saturated with oxygen at room temperature and heated to 1300 K for 30 sec before cesium adsorption. This equilibration procedure caused some zirconium to diffuse into the crystal, reducing its

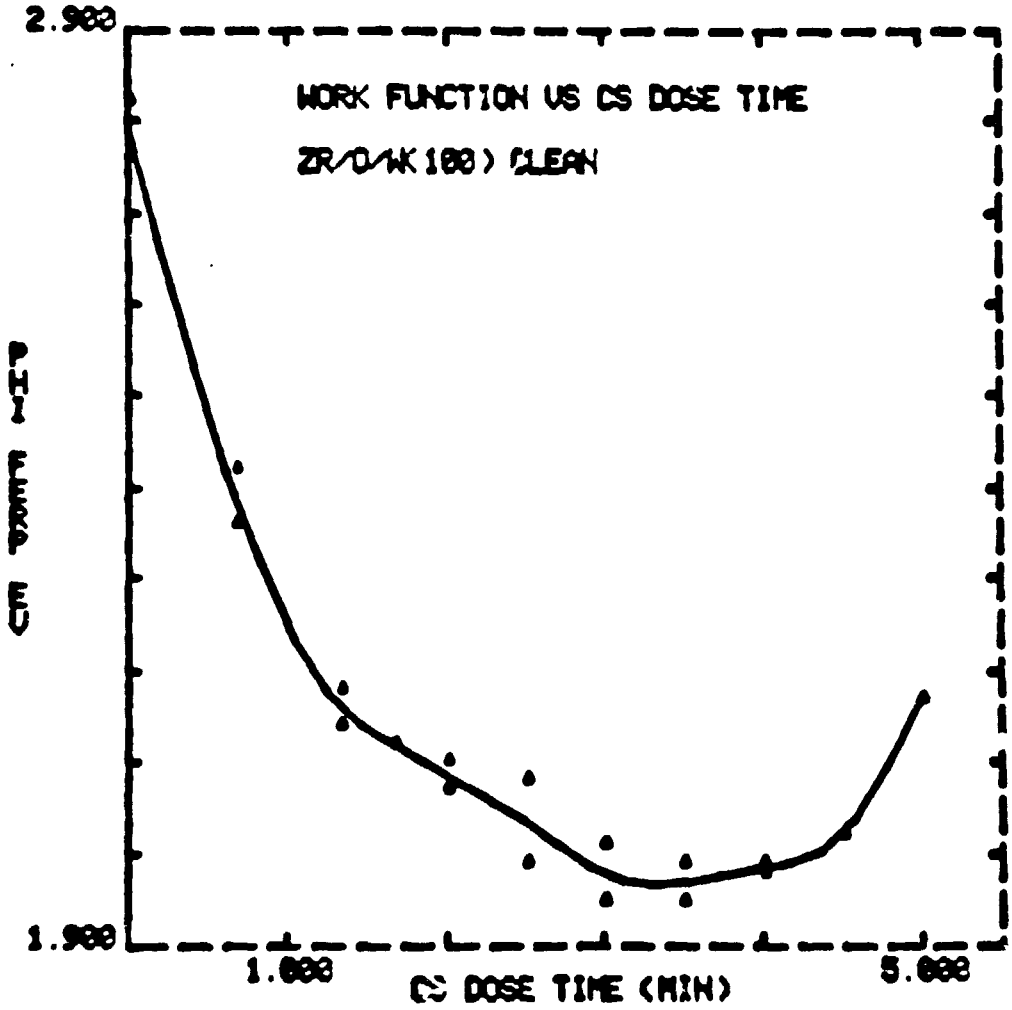

Figure 18. Variation of work function with Cs dose time, Cs on Zr/O/W(100) surface.

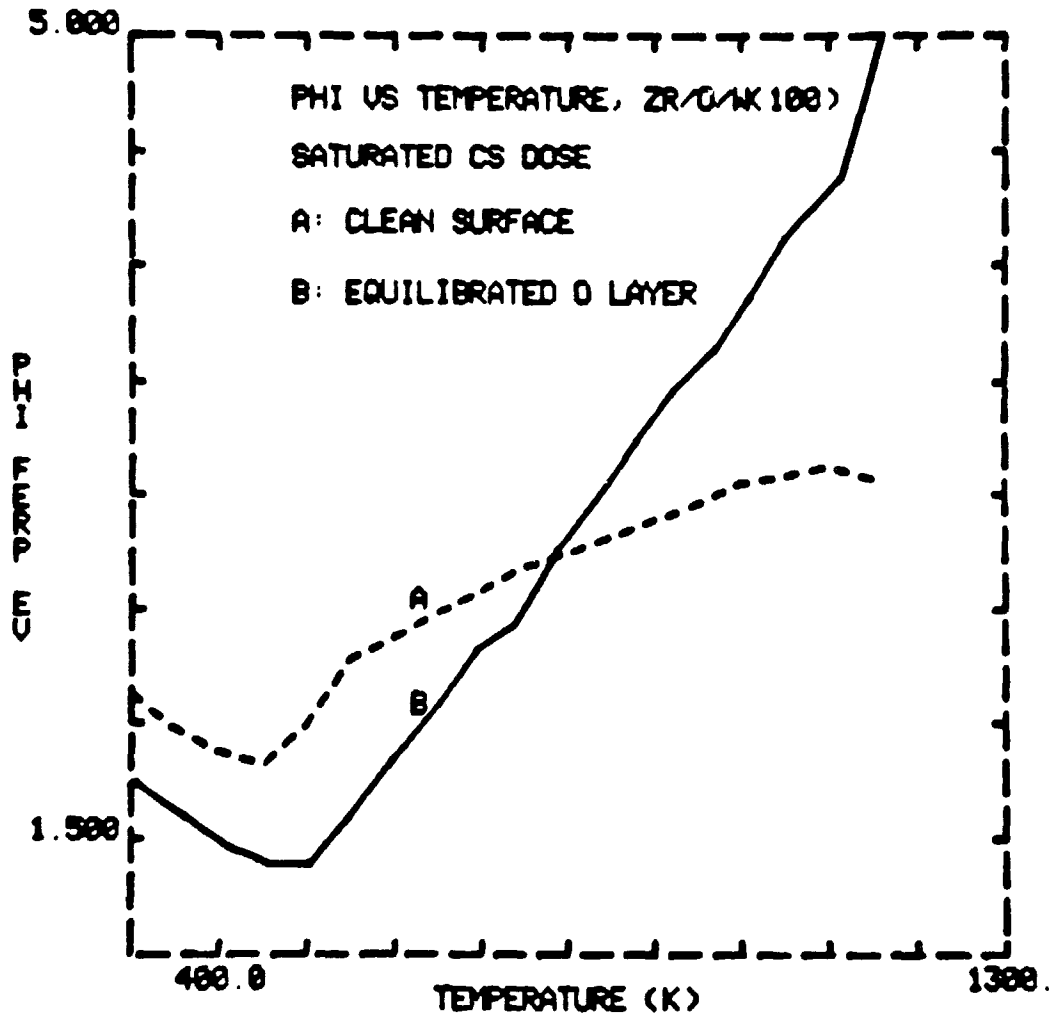

Figure 19. Change of work function with temperature during desorption of initially saturated Cs layers on Zr/O/W(100), clean and with a thermally equilibrated oxygen layer.

surface concentration. Therefore, although the thermally equilibrated surface may be stable with respect to heating, a non-equilibrated oxygen layer is not. The cesium desorption sequence consisted of a 2 min. heating at each successively higher temperature with a FERP measurement after each heating. Figure 19, curves A and B thus approximate quasiequilibrium Rasor plots for zero cesium pressure. The obvious criterion of desirability for converter applications in this type of plot is low work function at high temperature.

Swanson, et al.,[29] performed similar experiments for Cs desorption from W field emitters, the results of which are plotted in Figure 20 for comparison with the present work. These field emission data represent a weighted average over all planes of the field emitter tip (low work functions predominating). Since the various crystal planes exhibit different work function behavior, these weighted data approximate the lowest attainable work functions for cesium on tungsten at the indicated temperatures. Such results are likely to be better than those observed for any particular crystal plane over the entire temperature range. Comparison of Figures 19 and 20 suggests that, over much of the temperature range considered, a saturated oxygen layer on W (Figure 20 C), with adsorbed Cs, yields a lower work function than the Zr/O/W(100) surface treated in an equivalent way. Field emission microscopy measurements[29] show that the (211) planes are uniformly bright (low work function relative to other planes) over the entire temperature range, for curve C in Figure 20. No other plane is bright over the entire range.

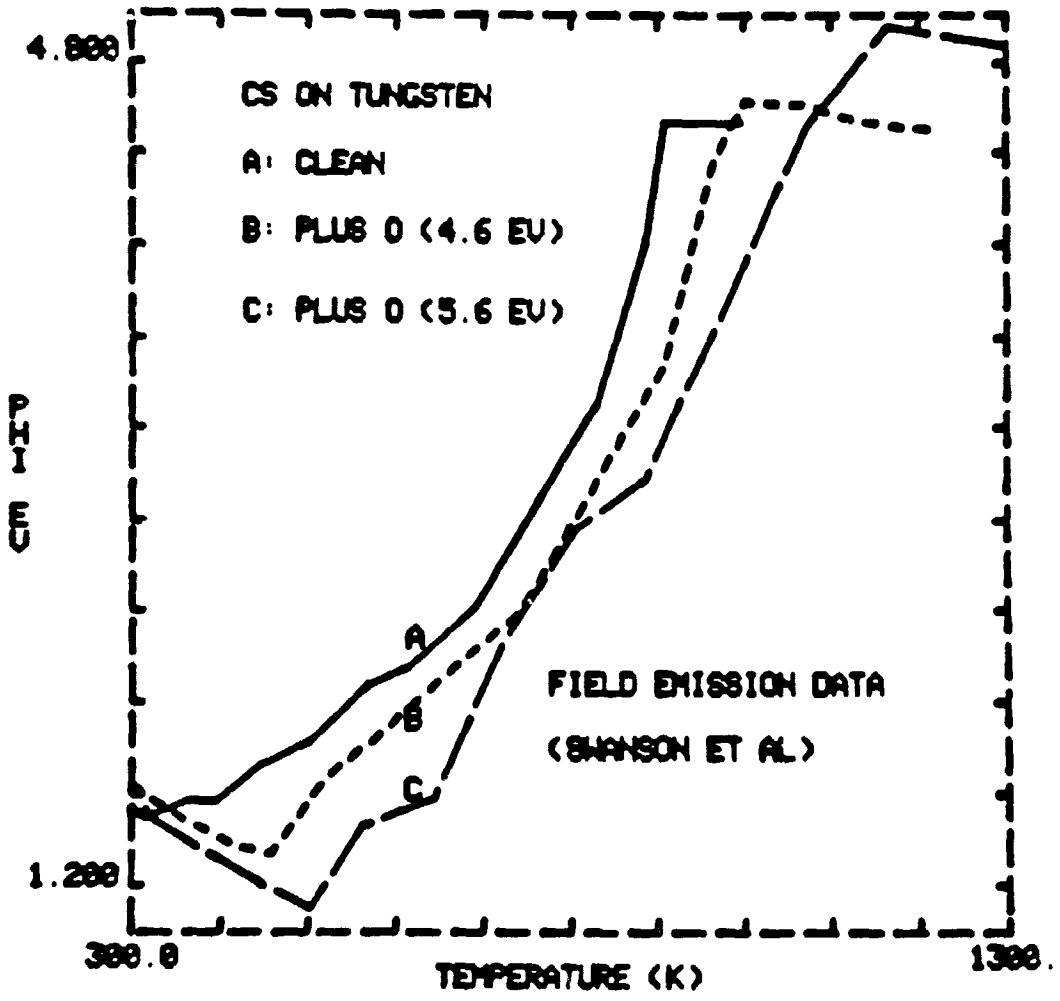

Figure 20. Variation of average work function with temperature after Cs adsorption to saturation on a clean, partly oxygen covered or fully oxygen covered W field emitter. Data from Ref. 29.

The curves in Figures 19 and 20 will be shifted toward higher temperatures with the introduction of cesium vapor, but the shift for each curve should be different, depending upon the particular binding energies of cesium on the various surfaces. We therefore also investigated the thermal desorption of cesium.

In Figure 21, cesium neutral desorption spectra are shown for three different initial surface conditions, with saturated coverage of cesium. These curves have been computer adjusted for the nonlinear heating rate used, so the relative magnitudes of peaks are correct. Desorption energies have been determined using the Redhead equation,[20] with allowance made for the nonlinear heating rate. The results are given in Table XIV, along with comparable data by Desplat[28] for Cs on clean and oxygen covered W(110). The table also includes the cesium zero coverage binding energy, that is, the terminal binding energy of the cesium as the coverage approaches zero.

These data show that, of the surfaces considered here, cesium is most strongly bound to W(110) with oxygen equilibrated or non-equilibrated. Second is the Zr/O/W(100) surface with a saturated, equilibrated oxygen layer. Then come non-equilibrated oxygen on Zr/O/W(100) and the clean Zr/O/W(100) in decreasing order of affinity for cesium.

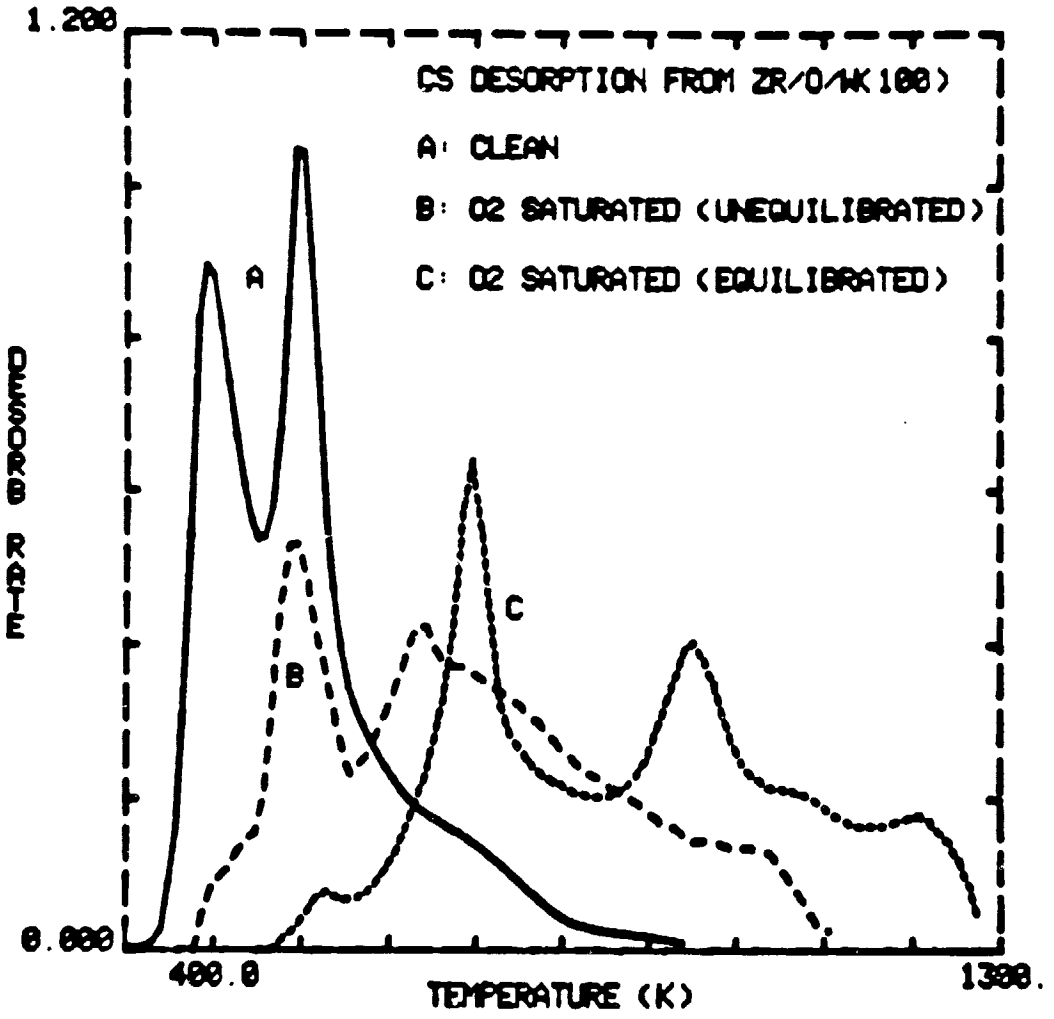

Figure 21. Desorption spectra of saturated Cs layers on Zr/O/W(100), clean and with thermally equilibrated and unequilibrated excess oxygen layers.

TABLE XIV

Desorption Energies of Neutral Cs from Various Surfaces (major peaks)

Surface	Desorption Energies (eV)	Zero Coverage Binding energy (eV)
1) Zr/O/W(100)		
a) clean	.97 ± .05	1.97 ± .2
	1.25 ± .05†	
b) oxygen saturated (non-equilibrated)	1.20 ± .05	2.63 ± .1
	1.56 ± .05†	
c) oxygen saturated (equilibrated 1300 K)	1.28 ± .05	3.14 ± .1
	1.72 ± .05	
	2.40 ± .05	
	2.77 ± .05†	
2) W(110)††		
a) clean	1.3†	3.1
b) 0.7 monolayer oxygen (unannealed)	.91	
	1.5†	3.9
c) "2-D oxide" (1 monolayer oxygen, annealed)	.91	3.86
	1.36	
	1.77	
	3.23	
	3.86	

†Above this energy, a continuum of values is present up to the zero coverage limit.

††Data of Desplat, Ref. 28.

V. Summary

The objective of this project is to fabricate, characterize and evaluate electrode materials that have the potential of significantly improving converter performance. Particular attention has been paid to the promising materials LaB_6 and Zr/W and Hf/W alloys, because of their low uncesiated work functions and low volatilities. The alloys W-.5% Hf and W-5% Hf were studied in detail, as was the model system Zr/O/W(100). Lanthanum-rich LaB_6 samples, $LaB_{5.74}$(100), (110) and (321), were characterized in the clean state. The effects of oxygen and cesium adsorption on the surface properties of the $LaB_{5.74}$(100) and the Zr/O/W(100) samples were investigated.

The clean work functions of $LaB_{5.74}$ surfaces have been found to be approximately the same as the corresponding faces on $LaB_{5.86}$. The effect on work function of stoichiometry in this range is apparently small, but the La vaporization energy is significantly lower in the more La-rich case. The $LaB_{5.74}$(321) surface probably facets at high temperature because the effective thermionic work function is significantly lower than the room temperature FERP work function for that surface. Heating the (100) surface above 1000 K in an oxygen pressure greater than $\sim 5 \times 10^{-8}$ torr causes volatile boron oxide species to evaporate. The major oxide product is B_2O_2 in the temperature range $1000 \lesssim T \lesssim 1550$ K at an oxygen pressure of 1×10^{-6} torr. Cesium adsorption on clean and oxygen covered $LaB_{5.74}$(100) surfaces yielded work function minima of $\sim$ 2.0 and 1.3 eV, respectively. Thermal desorption of cesium in these two cases

was complete at ~ 900 and 1100 K, respectively.

The Zr/O/W(100) surface has been studied in detail. The low work function (ϕ = 2.6 eV) surface is stable to T > 1800 K in vacuum. Oxygen contaminates the surface, increasing the work function and, at elevated sample temperatures, causes surface Zr to diffuse into the bulk of the crystal. Heating at 2000 K in vacuum re-establishes the Zr surface coverage and the low work function. Transport of Zr and O into and out of the bulk appears to proceed as diffusion of a Zr-O complex, since the activation energies of diffusion of the two species are identical within experimental error. Polycrystalline W-.5% Hf and W-5% Hf alloy samples exhibited similar diffusion behavior. The thermionic work function minima obtained for these materials were higher than that observed for the Zr/O/W(100) system, since exposed planes other than (100) exhibit less work function lowering due to Zr or Hf. Further work on these alloys should concentrate on optimization of Zr or Hf content and development of the maximum density of (100) surface planes.

Cesium adsorption on the W-.5% Hf and W-5% Hf surfaces yielded FERP work function minima of 1.65 and 1.85 eV, respectively. More detailed studies of cesium adsorption on the well characterized Zr/O/W(100) surface showed work function minimia of ~ 1.9 eV on the ϕ = 2.6 eV initial surface and ~ 1.4 eV on the surface with excess adsorbed oxygen. This latter surface changed during heating, because of diffusion of the Zr-O complex into the bulk. Studies of cesium desorption from the Zr/O/W(100) surface showed terminal binding

energies of 2.0 ± .2 eV on the initial low work function surface, 2.6 ± .1 eV on that surface saturated with oxygen at 300 K and 3.1 ± .1 eV on a thermally equilibrated (1300 K) oxygen layer.

References

1. J. F. Morris, "High Efficiency, Low Temperature Cesium Diode with Lanthanum-Hexaboride Electrodes," NASA TMX-7149 (1974).
2. R. W. Strayer, W. Mackie and L. W. Swanson, Surface Science 34 (1973) 225.
3. E. Storms and B. Mueller, J. Phys, Chem. 82 (1978) 51.
4. L. W. Swanson and N. A. Martin, J. Appl. Phys. 46 (1975) 2029.
5. L. R. Danielson and L. W. Swanson, Surface Science 88 (1979) 14.
6. J. F. Morris (private communication).
7. M. Noack, M.S. Thesis (Iowa State University, Ames, Iowa 1979).
8. L. W. Swanson, D. R. McNeely and M. Gesley, NASA CR-159649, August 1979.
9. E. B. Bas, P. Hafner and S. Klauser, Proc. 7th Intern. Vac. Congr. and 3rd Intern. Conf. Solid Surfaces (Vienna 1977), 881; Appl. Surface Science 3 (1979) 356.
10. L. W. Swanson and T. Dickinson, Appl. Phys. Lett. 28 (1976) 578.
11. H. Yamouchi, K. Takagi, I. Yuito and U. Kawabe, Appl. Phys. Lett. 29 (1976) 578.
12. C. Oshima, E. Bannai, T. Tanaka and S. Kawai, J. Appl. Phys. 48 (1979) 3925.
13. P. Schmidt, L. D. Longinotti, D. C. Joy, S. D. Ferris, H. J. Leamy and Z. Fisk, J. Vac. Sci. Technol. 15 (1978) 1554.
14. A. Berrada, J. Mercurio, J. Etourneace and P. Hagenmuller, Rev. Int. hautes Tempér. Réfract. Fr. 15 (1978) 115.
15. L. W. Swanson, M. Gesley and D. R. McNeely, Interim Report #2, NASA Grant No. NSG-3054.

16. E. K. Storms and B. A. Mueller, J. Appl. Phys. 50 (1979) 3691.

17. G. A. Kudintseva, G. M. Kuznetsova, E. G. Mamedov, G. A. Meerson and B. M. Tsarez, Izv. Akad. Nauk. SSSR Neorg. Mater. 4 (1968) 49.

18. L. W. Swanson and D. R. McNeely, Surface Science 83 (1979) 11.

19. B. Goldstein and D. J. Szostak, Surface Science 74 (1978) 461.

20. P. A. Redhead, Vacuum 12 (1962) 203.

21. F. A. Cotton and G. Wilkinson, Advanced Inorganic Chemistry (Wiley-Interscience, 1962).

22. L. W. Swanson, J. Vac. Sci. Technol. 12 (1975) 1228.

23. P. R. Davis, Surface Science 91 (1980) 385.

24. G. E. Hill, I. Marklund, J. Martinson and B. J. Hopkins, Surface Science 24 (1971) 435.

25. H. Shelton, Phys. Rev. 107 (1957) 1553.

26. P. Kisliuk, Phys. Rev. 122 (1961) 405.

27. C. J. Bennette, R. W. Strayer, L. W. Swanson and E. C. Cooper, NASA CR-54704 (1966).

28. J. L. Desplat, NASA CR-152272 (1979).

29. L. W. Swanson, R. W. Strayer, E. C. Cooper and F. M. Charbonnier, Annual Report, NASA Contract No. NASw-458 (1963).